Review

Xi Gao and Tie Jun Cui*

Spoof surface plasmon polaritons supported by ultrathin corrugated metal strip and their applications

Abstract: In this review, we present a brief introduction on the spoof surface plasmons supported on corrugated metallic plates with nearly zero thickness. We mainly focus on the propagation characteristics of spoof surface plasmon polaritons (SPPs), excitation of planar SPPs, and several plasmonic devices including the bending waveguide, Y-shaped beam splitter, frequency splitter, and filter. These devices are designed and fabricated with either planar or conformal plasmonic metamaterials, which are validated by both full-wave simulations and experiments, showing high performance. We also demonstrate that an ultrathin textured metallic disk can support multipolar spoof localized surface plasmons, either with straight or curved grooves, from which the Fano resonances are also observed.

Keywords: conformal surface plasmons; Fano resonance; localized surface plasmons; plasmonic devices; surface plasmon polaritons.

DOI 10.1515/ntrev-2014-0032 Received October 28, 2014; accepted March 13, 2015

1 Introduction

Surface plasmon polaritons (SPPs) occur at an interface between two materials with opposite permittivity and decay exponentially in the transverse direction [1, 2].

*Corresponding author: Tie Jun Cui, State Key Laboratory of Millimeter Waves, Department of Radio Engineering, Southeast University, Nanjing 210096, People's Republic of China, e-mail: tjcui@seu.edu.cn

Xi Gao: State Key Laboratory of Millimeter Waves, Department of Radio Engineering, Southeast University, Nanjing 210096, People's Republic of China; and School of Information and Communication, Guilin University of Electronic Technology, Guilin 541004, People's Republic of China Attributing to remarkable features and huge application potentials [3-10], SPPs have attracted extensive attentions and have been intensively investigated. At optical frequencies, metals behave like plasmas with negative permittivity, which makes SPPs be highly confined to the interface of metal and air (or metal and dielectric) and propagate along the surface. SPPs can overcome diffraction limit and realize miniaturized photonic components and integrated circuits due to their highly localized feature, which makes it widely used in nano-photonics and optoelectronics [4, 11-14]. However, as the frequency goes downward to microwave and terahertz regions, the natural SPPs do not exist on smooth metal surfaces because of infinite dielectric constant of metal [1]. Instead, Sommerfeld or Zenneck surface waves can be supported on the surface, which have weak confinements and short propagation distances [15–17].

Recently, structured surfaces (or plasmonic surfaces), which are formed by decorating periodic arrays of subwavelength grooves, holes, or blocks on metal surfaces, are proposed to support the surface waves that in many respects mimic or "spoof" real surface plasmons [18–24]. These spoof surface plasmons open up the terahertz and microwave to plasmonic studies for their potential applications [25–30]. On the other hand, the conversions from spatial propagating waves or guided waves to SPPs have been extensively studied to further promote the practical application of SPPs [25, 31–35], but coupling efficiencies are very limited. Though the spoof SPPs have many desirable features for their extensive applications, they have a major limitation associated with the excitation with low efficiency and inherent three-dimensional (3D) geometry.

In order to obtain compact SPP waveguides and components, the thickness has been reduced to subwavelength scales [35–38]. It has been shown that the 3D plasmonic waveguides with subwavelength thickness can support good SPP waves, but are still inconvenient to be integrated. In recent years, a novel plasmonic waveguide with nearly zero thickness has been proposed [39–42],

which can overcome the above-mentioned difficulties. Furthermore, high efficiency and wideband conversions from guided waves to spoof SPP have been proposed [43, 44] to develop practical function devices.

In this paper, we briefly review our recent efforts in studying the fundamental physical properties of such plasmonic metamaterials and realizing certain applications. This review is organized as follows. We first introduce the SPP characteristics of planar plamsonic waveguides and components in Section 2. Section 3 presents the conformal properties of our plasmonic metamaterials. The excitations of planar SPPs are illustrated in Section 4. We then demonstrate the spoof localized surface plasmons (LSPs) in an ultrathin plasmonic particle in Section 5. The conclusion of this review is given in Section 6.

2 Planar plasmonic waveguides and components

The proposed planar plasmonic metamaterial is a combshaped and free-standing structure [39, 40], as the inset illustrated in Figure 1. A periodic array of edge grooves with depth d, width a, period p, and height h is corrugated on a perfectly conducting metal strip with thickness t. Using the full-wave finite-element method, we calculate the dispersion curves of the TM-polarized waves propagating in the x direction along the corrugated metal strip.

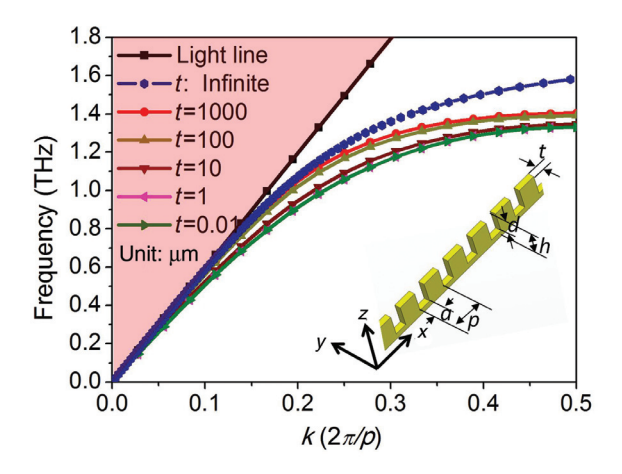


Figure 1: Dispersion curves of the spoof SPPs in plasmonic metamaterial with different thickness. The black line denotes the light line, the blue line shows the dispersion curve of the corrugated metal plate with infinite thickness in the y direction, and the other lines correspond to five values of thickness: t=1000, 100, 10, 1, and 0.01 μ m. The inset displays the corrugated metal strip with p=h=50 μ m, d=40 μ m, and d=20 μ m. Reproduced from [39] with permission.

Figure 1 shows the dispersion curves of the fundamental mode for different thickness t. Here, we choose $p=50 \mu m$, $a=20 \mu \text{m}$, $d=40 \mu \text{m}$, $h=50 \mu \text{m}$, and six values of thickness t (infinite, 100, 10, 1, 0.1, and 0.01 mm), respectively. It is clearly seen that the dispersion curve further deviates from the light line, and the asymptotic frequency becomes lower when the thickness t decreases, implying tight confinement of surface waves on thinner corrugated metal strip. Especially when the thickness is below 1 µm, the dispersion curve keeps unchanged, which suggests that the plasmonic modes are insensitive to the variation of thickness. Even if the thickness of metal strip tends to zero, the surface wave still can be stronger confined around them. Here, we focus on our studies on corrugated thin metal film with nearly zero thickness (t=0.01 μ m), which is termed as the planar plasmonic metamateiral. As illustrated in Figure 1, in the frequency ranging from 0.7 THz to 1.2 THz, the wave vector of SPP is bigger than the wave number of light line, implying strong confinement of SPPs. Compared with 3D structure, our structure exhibits a crucial advantage – it is convenient to integrate in a plane to form a plasmonic circuit.

Using the full-wave simulation method, we have demonstrated the confinement and propagation characteristics of spoof SPPs on the planar plasmonic metamateiral by observing electric field patterns on different planes. Figure 2A illustrates the distribution of electric field (E_{-}) on an x-y plane 2 µm above the planar plasmonic waveguide with 800 µm long at 1.0 THz, which implies excellent SPP propagation. Figure 2B and C shows detailed SPP modes on the y-z plane located at $x=500 \mu m$ and 7500 μm , and Figure 2D and E displays the field distributions of SPP modes along two orthogonal cuts (dashed line in Figure 2B and C). These figures show the following unique features of planar plasmonic metamaterial: (1) Along the propagating (x) direction, SPPs propagate nearly lossless and keep almost unchanged modal shapes; (2) Along the vertical (z)direction, SPPs are highly confined around the plasmonic metamaterial, whose fields decay exponentially on both sides of the film; (3) along the transverse (y) direction, the field values keep constantly large in the vicinity of film edges and decay exponentially beyond the vicinity. These features make the planar plasmonic metamaterial confine the broadband terahertz waves in two orthogonal (y and z) directions and guide the waves to propagate in the third (x) direction.

According to the scale invariance of classical electromagnetism, the dispersion relations of the planar plasmonic metamaterial can be scaled down to the microwave frequency. Therefore, the following work in this review paper is mainly focused on microwave frequency. To

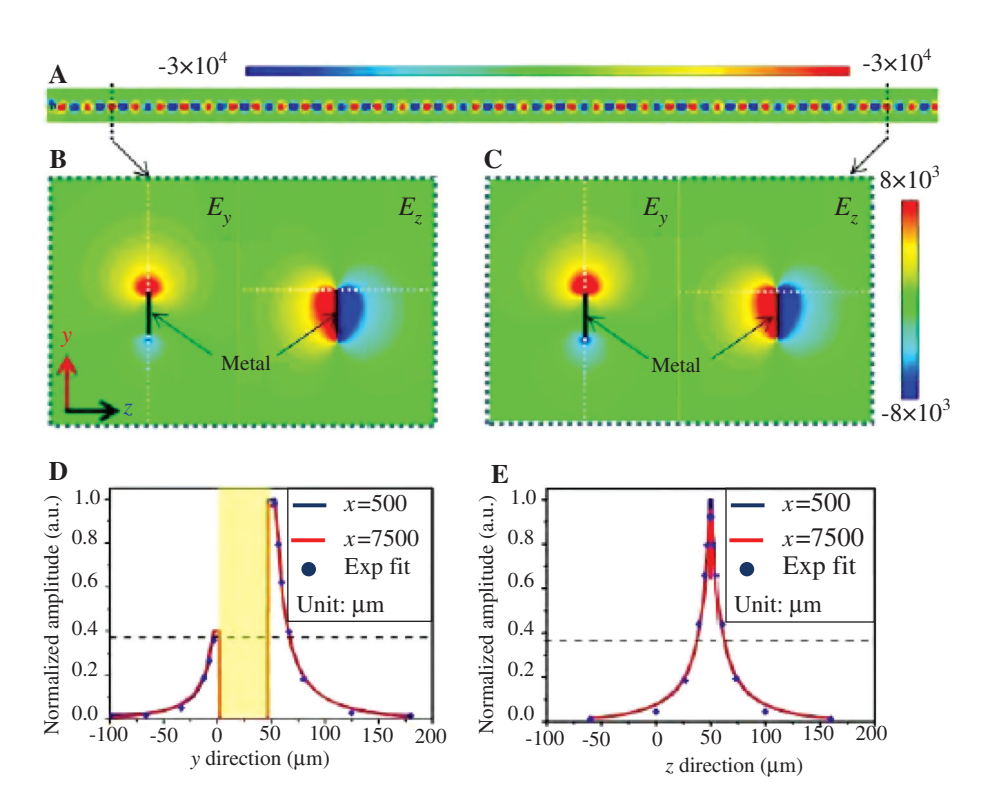


Figure 2: Numerical simulation results of the planar plasmonic waveguide in terahertz region. (A) The electric field (E) of the SPP propagation at 1.0 THz, in which the thickness (t) and the length (L) of the plasmonic waveguide are designed as 0.01 µm and 8000 µm, respectively. (B, C) Distributions of E_{μ} and E_{μ} components on the y-z plane located at $x=500~\mu m$ and $7500~\mu m$ along the plasmonic waveguide, which denote the transverse size of SPP mode. (D, E) The normalized magnitude of E, and E, along the white-dot lines marked in (B) and (C). Reproduced from [40] with permission.

verify the excellent SPP performance of ultrathin corrugated metal strip by experiment method, we scale up the geometric parameters by 100 times, namely, p=h=5 mm, d=4 mm, and a=2 mm, which makes the SPPs propagate in the frequency ranging from 7 GHz to 11 GHz. Using the printed circuit board (PCB) technology, a corrugated copper strip 200 mm long, 5 mm wide, and 0.018 mm thick is etched on a 0.1-mm-thick substrate with dielectric constant 2.65 and loss tangent 0.001 (Figure 3F). Two monopoles are used as the source and detector, respectively. The detector is fixed at 1 mm above the sample and moves on the x-y plane to scan the E_z field, and the magnitude and phase information of E_z field is recorded by the Agilent N5230C vector network analyzer. Figure 3A-E represents the measured electric fields at specifies frequencies: 7 GHz, 8 GHz, 9 GHz, 10 GHz, and 11 GHz, respectively, which demonstrate that the planar plasmonic metamaterials can efficiently confine broadband spoof SPPs and maintain a long propagation distance.

According to reference [1], the confinement of SPPs is relation to the value of wave number (*k*). For a large wave number (*k*) in the dispersion curve, the spoof SPP waves can be tightly bound by structured surface and propagate with very low loss. In the opposite regime of small wave vectors k, however, the spoof SPP waves extend over many wavelengths into free space and display the delocalized nature. Especially for Sommerfeld-Zenneck waves (k is very close to k_0), they have very weak confinement on the surfaces and short propagating distance. There is an effective method to realize strong confinement of the surface waves in regime of small wave vectors [41], in which two corrugated metal plates located in opposite directions are used to form a plasmonic waveguide, as shown in Figure 4B. The two corrugated metal plates having the same width (t), depth (h), and periodicity (d) of groove are spaced by a distance (w). The full-wave finite-element method is employed to calculate the dispersion curves of single and double gratings, as illustrated in Figure 4C. We observe that the dispersion curve of the double grating has a similar behavior as that of the single grating except the slightly lower asymptotic frequency. The difference is that the double grating can simultaneously confine the spoof SPP wave in two (-y and +y) directions, which makes very low radiation loss of spoof SPP (especially for Sommerfeld-Zenneck waves) and realizes high-efficiency propagation. The high-efficiency SPP propagation has

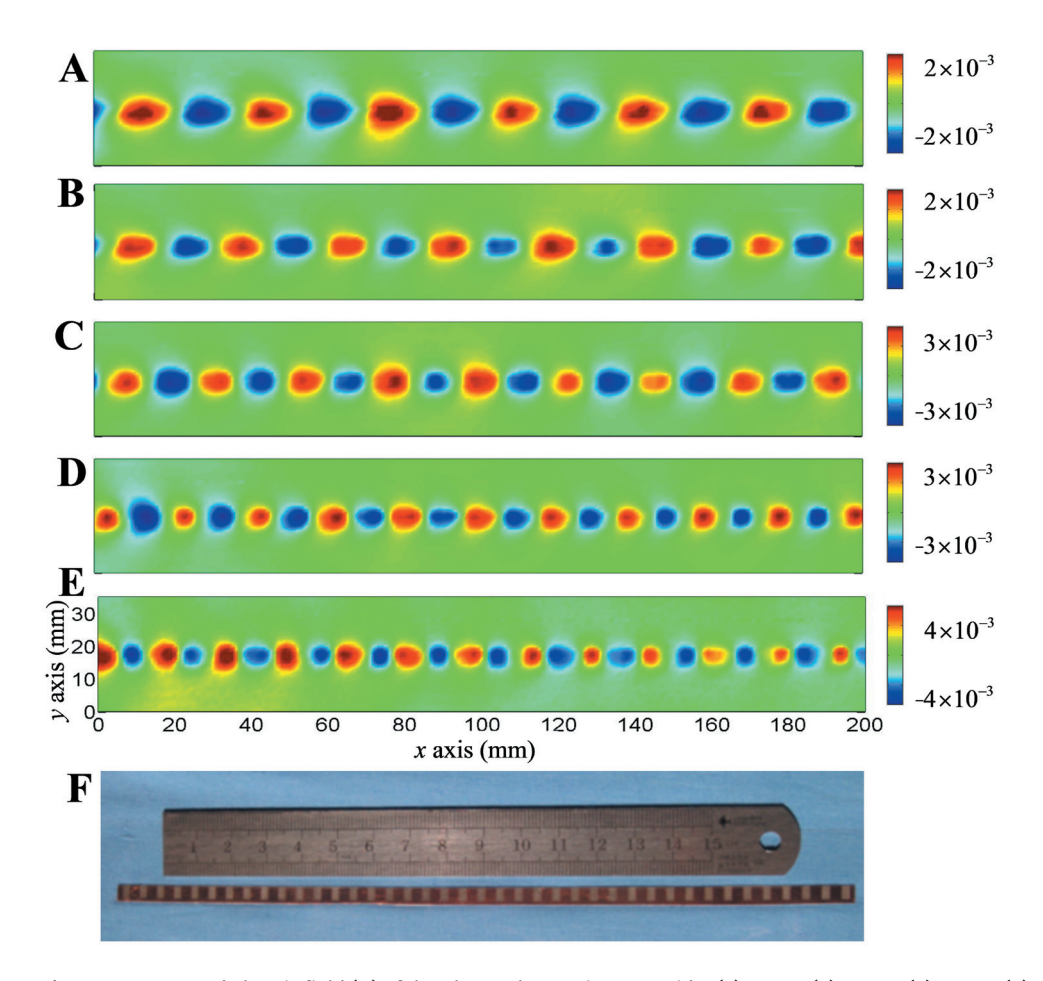


Figure 3: Measured electric field (E_z) of the planar plasmonic waveguide. (A) 7 GHz; (B) 8 GHz; (C) 9 GHz; (D) 10 GHz; (E) 11 GHz; (F) photo of fabricated planar plasmonic waveguide, in which the 0.018-mm-thick copper is printed on the 0.15-mm-thick substrate. The geometric parameters of groove are p=h=5 mm, d=4 mm, and a=2 mm. Reproduced from [40] with permission.

been verified by numerical calculation of transmission loss, as illustrated in Figure 4D. It is clearly seen that the loss of spoof SPPs in the double grating is obviously lower than that in the single grating. Especially for the Sommerfeld-Zenneck waves with k close to $k_{\rm o}$, the loss in double grating is still very low, which implies that the double grating can effectively confine the Sommerfeld-Zenneck waves and, hence, extend the transmission bandwidth of the spoof SPP wave. Based on the plasmonic waveguide, an ultra-wideband plasmonic filter with high performance can be designed [41].

An interesting physical phenomenon is that the planar plamsonic waveguide can support dual-band spoof SPP propagation by etching periodic grooves with two different depths on an ultrathin metallic strip [42]. The periodic deep and shallow grooves can independently couple EM waves in two different frequency bands to form dual-band spoof SPP propagation. As an example, we have designed a composite-periodic plasmonic waveguide, as shown in Figure 5A. The

groove width and periodicity are designed as w=1 mm and p=5 mm, respectively, and the depths of deep and shallow grooves are denoted as d_1 and d_2 , respectively. The thickness of the metal plate is t=0.018 mm. Figure 5B illustrates the dispersion relation of the plasmonic waveguide with double periodic grooves, in which the dashed black line is the light line in free space, the solid black and red lines correspond to the shallow grooves with d_3 =5 mm and 5.5 mm for fixed d_4 =11 mm, while the solid pink and green lines correspond to the deep groove with d_1 =11 mm and 11.5 mm for a fixed d_2 =5 mm. It is clearly seen that the two SPP modes are supported by the corrugated metal strip with double periodic grooves. Figure 5C and D gives the field patterns of E_z field in a y-z plane for the two SPP modes, and Figure 5E represents the E_z field distribution along the observed line (see Figure 5A) above the surface of the plasmonic waveguide. From these figures, we obtain the following interesting characteristics: (1) The plasmonic metamaterial can simultaneously support dual-band SPP propagation, and the operation

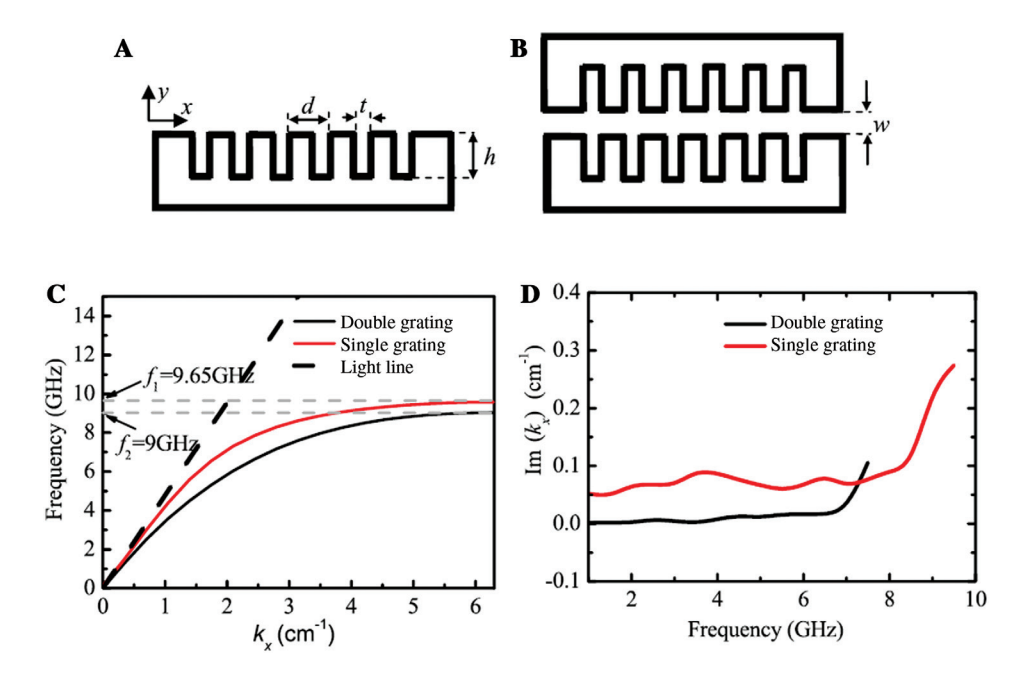


Figure 4: Schematic pictures of single and double ultrathin corrugated metal plates and their dispersion curves. (A, B) Single and double corrugated metal plates, respectively, in which the groove depth, width, and periodicity are designed as h, t, and d, respectively. The gap between the double corrugated metal plates is denoted as w. The parameters h, t, d, and w are defined as 6.5 mm, 1 mm, 5 mm, and 1.5 mm, respectively. (C) Dispersion curves of single and double gratings, in which the red and black solid lines correspond to the single and double gratings, respectively, and the black dashed line denotes the light line in free space. (D) Im(k) as a function of frequencies for double and single grating. Reproduced from [41] with permission.

frequencies of the dual-band SPPs can be independently manipulated by the depth of deep and shallow grooves (see Figure 5A), respectively; 2) The two SPP modes have similar E_z field distribution in the transverse section (see Figure 5C, D), and their E_z fields are consistent with the single periodic grooves (see Figure 5E), implying strong confinement of dual-band SPP.

Using the dual-band propagation characteristic and little bend loss, we can design a novel plasmonic device with compacted structure, such as frequency splitter. In Figure 6A, we give the photo of a fabricated sample of a frequency splitter [42], in which the geometric parameters of single- and double-periodic grooves are coincident with that shown in Figure 5, and the other parameters are designed as t=2 mm, $L_1=L_2=70$ mm. Owing to the dual-band spoof SPP propagation in the left plasmonic waveguide and their similar dispersion curves and mode patterns to the single periodic grooves in the right side, the two SPP waves in the low (high)frequency band can independently couple to the right lower (upper) branch. For such a frequency splitter, the simulation-normalized electric fields (E) at low (5.2)GHz)- and high (10.2 GHz)-frequency bands, which correspond to the central frequencies of the two SPP bands supported by the left straight plasmonic waveguide, are

shown in Figure 6B-E, demonstrating the excellent performance. Compared with the frequency splitter shown in Ref. [36], our structure is more compact and convenient in practical application.

Another advantage of our plasmonic metamaterials is that they have very low bend loss, which have potential application to produce many kinds of function devices. Based on these proposed planar plasmonic metamaterials, we have designed a 90° SPP bend and a 60° Y-shaped beam splitter [40]. Figure 7A and B illustrates the photos of fabricated 90° bending plasmonic waveguide and 60° Y-shaped beam splitter, respectively, in which the geometric parameters of groove are consistent with that in Figure 3. The 90° bend is formed by two straight SPP waveguides connected by a curved waveguide along a circular arc of radius 30 mm, and the designed beam splitter consists of two symmetric S-bends, each of which is composed of three straight planar plasmonic waveguides with 30° bending angle. The measured results of E_z fields from 7 GHz to 11 GHz are demonstrated in Figures 8 and 9. From these figures, we observe that the SPP waves travel along the circular arc in a 90° bend and are divided equally into the output arms in a Y-shaped splitter with very low loss, implying the excellent performance over a large frequency range.

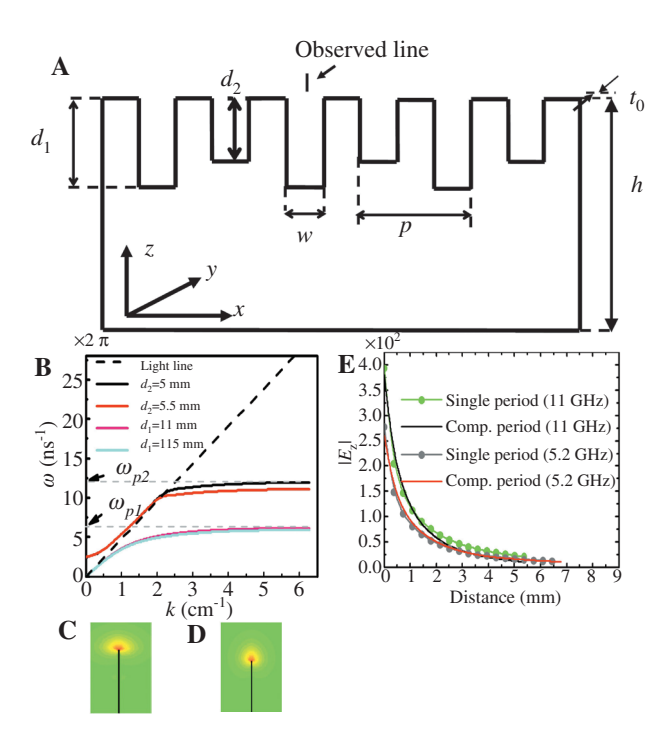


Figure 5: (A) The sketch of the dual-periodic planar metamaterial. (B) Dispersion curves of the dual-periodic grooves with depth d_1 and d_2 , where w=1 mm, p=5 m, and h=40 mm. (C, D) The mode patterns of E_2 field of the dual-periodic grooves. (E) The E_2 field distribution along the observed line [see (A)] above the composite periodic grooves and single periodic grating at 5.2 GHz and 11 GHz, respectively. Reproduced from [42] with permission.

3 Conformal surface plasmons

Propagation of EM waves along a conformal surface with low loss is very important and interesting in many fields. Attributing to the ultrathin nature of these proposed

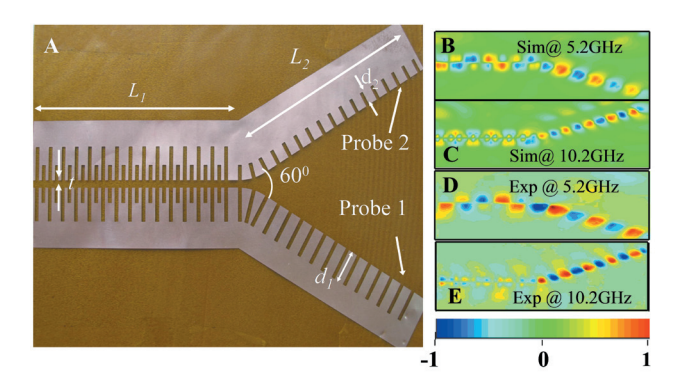


Figure 6: (A) Photo of the fabricated planar frequency splitter, which is composed of a straight composite periodic grating and two single-periodic grating branches, where $L_1 = L_2 = 70$ mm, t = 2 mm, $d_1 = 11$ mm, and $d_2 = 5$ mm. (B–E) Simulated and measured E_2 field distributions of the frequency splitter at 5.2 GHz and 10.2 GHz. Reproduced from [42] with permission.

corrugated metallic strips, we can easily make flexible SPP waveguide and components [40]. Based on the standard PCB fabrication process on a three-layered flexible copper clad laminate (FCCL) consisting of a single layer of polyimide and an electrolytic copper clad sheet connected with the epoxy adhesive, we have fabricated the corresponding plasmonic metamaterial, as illustrated in Figure 10, in which the thickness of polyimide, adhesive, and copper foil layer are 12.5 µm, 13 µm, and 18 µm, respectively, and hence, the total thickness of the film is 43.5 µm, which is much smaller than the working wavelength in the microwave frequency. As the fabricated samples are ultrathin and flexible, they can be wrapped around curved surfaces and, therefore, are very well suited for their incorporation into arbitrarily curved surfaces to mould the flow of conformal surface plasmons (CSPs).

In order to demonstrate CSP propagation on arbitrarily curved surfaces, we designed several typical structures based on FCCL films, in which the geometrical parameters of corrugated FCCL thin films are designed as d=5 mm, a=2 mm, h=2 mm, and w=5 mm (see Figure 11). These geometrical parameters make the plasmonic waveguide operate in microwave with the center frequency of 10 GHz. We consider the CSP propagation on a non-planar surface, which can be randomly fabricated using foam with a very low dielectric constant. Figure 11A-D illustrates the design model and the photo of the fabricated sample for two curved (S-bending and cubical) surfaces, on which the comb-shaped metal strip is pasted on the foam. For S-bending plasmonic waveguide, the simulation and measurement electric fields (E_{α}) at 10 GHz are demonstrated in Figure 12A-D, while for the cubical plasmonic waveguide, the electric field (E_{\cdot}) patterns are displayed in Figure 12E–F. These figures demonstrate that the amplitude of the electric field of CSPs is almost constant along both the curved surfaces, implying very small bending loss. Especially for a cubical surface, CSPs are creeping through a 90° corner smoothly with relatively low bending loss. Such excellent performance does not take place in the standard SPPs, spoof SPPs, and even in the conventional microwave waveguide (bulk and microstrip). More importantly, our ultrathin plasmonic waveguide can easily be fabricated into a spiral and a 3D helix structure, along which the SPP waves still have very little propagation loss [40].

4 Excitations of planar SPPs

Owing to the excellent SPP propagation characteristic of the proposed plasmonic metamaterial, it is possible to achieve plasmonic functional integrated circuits at

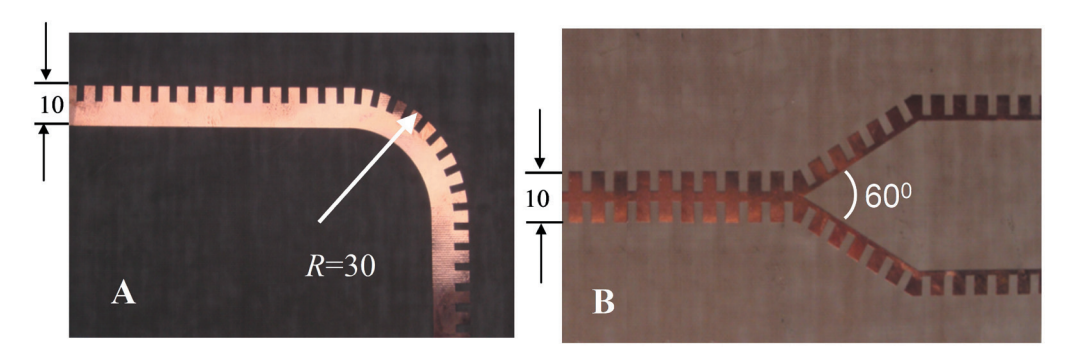


Figure 7: Photos of fabricated planar plasmonic 90° bend and Y-shaped beam splitter. (A) The 90° bend, (B) Y-shaped beam splitter. Reproduced from [40] with permission.

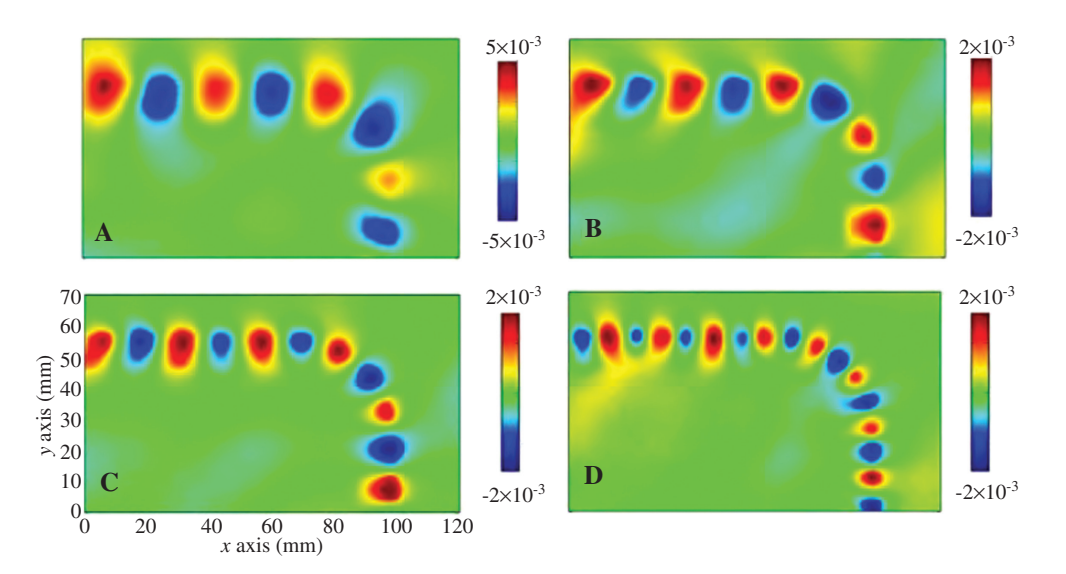


Figure 8: Measurement results of electric fields (E) of the planar plasmonic 90° bend in frequency ranging from 7 GHz to 11 GHz. (A) 7 GHz; (B) 8 GHz; (C) 9 GHz; (D) 11 GHz. Reproduced from [40] with permission.

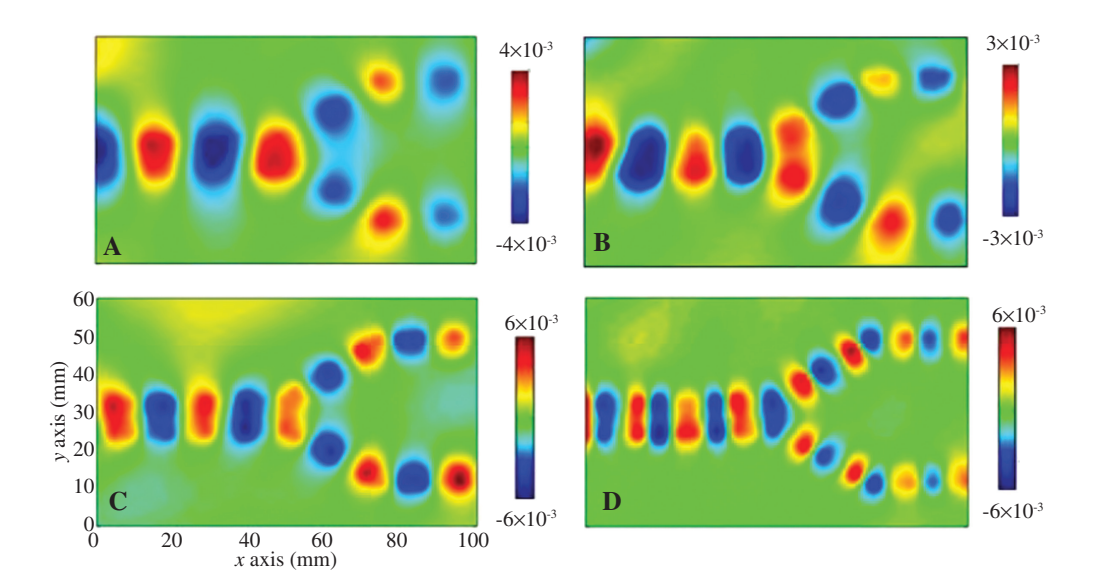


Figure 9: Measurement results of electric field (E) of the planar plasmonic beam splitter in frequency ranging from 7 GHz to 11 GHz. (A) 7 GHz; (B) 8 GHz; (C) 9 GHz; (D) 11 GHz. Reproduced from [40] with permission.

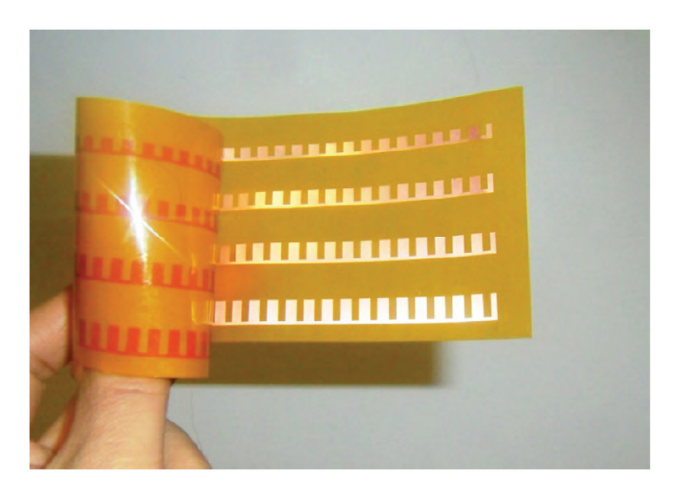


Figure 10: The fabricated sample of the flexible and ultrathin plasmonic metamaterials using FCCL. Reproduced from [40] with permission.

microwave and THz frequencies. However, the plasmonic waveguide is usually to be connected to the conventional microwave or THz circuits, which makes it very necessary to convert the guided waves supported by the conventional transmission lines to plasmonic waveguide with high efficiency. From the dispersion of spoof SPPs (see Figure 1), we know that the dispersion curve of the spoof SPP wave deviates from the light line, implying that the vector $k > k_0$. Therefore, there is a serious mismatch between the wave vector of spoof SPPs and that in free space. The mismatching of wave vectors makes it very difficult to feed EM energies into, and extract signals from, the plasmonic waveguide directly. In this section, we mainly review two

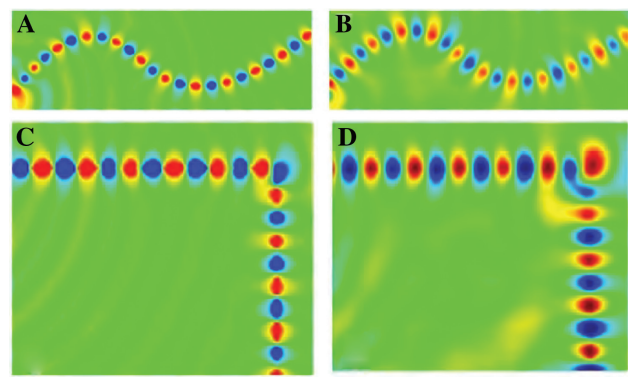


Figure 12: Simulation and experiment electric field distribution (E_z) at 10 GHz. (A) and (B) illustrate the simulation and measurement results for the S-bending surface, respectively. (C) and (D) represent the simulated and measured results for cubical surface, in which CSPs creep through the sharp corner smoothly.

kinds of spoof SPP converters from CPW, microstrip to plamsonic waveguide.

The first proposed CPW spoof SPP converter is illustrated in Figure 13 [43], in which the whole structure is divided into three regions. The first region (I) is CPW (see Figure 13B), which supports the quasi-transverse electric and magnetic (TEM) mode with wave vector k_0 . To obtain a 50- Ω impedance, the dimensions of CPW are designed as H=5 mm, W=25 mm, and W=0.4 mm. Region III is the corrugated metallic strip, which is a plasmonic transmission line supporting the spoof SPP mode with wave vector W=0.4 mm, width, and depth of grooves are designed as W=0.4 mm, W=0.4 mm, and W=0.4 mm, respectively.

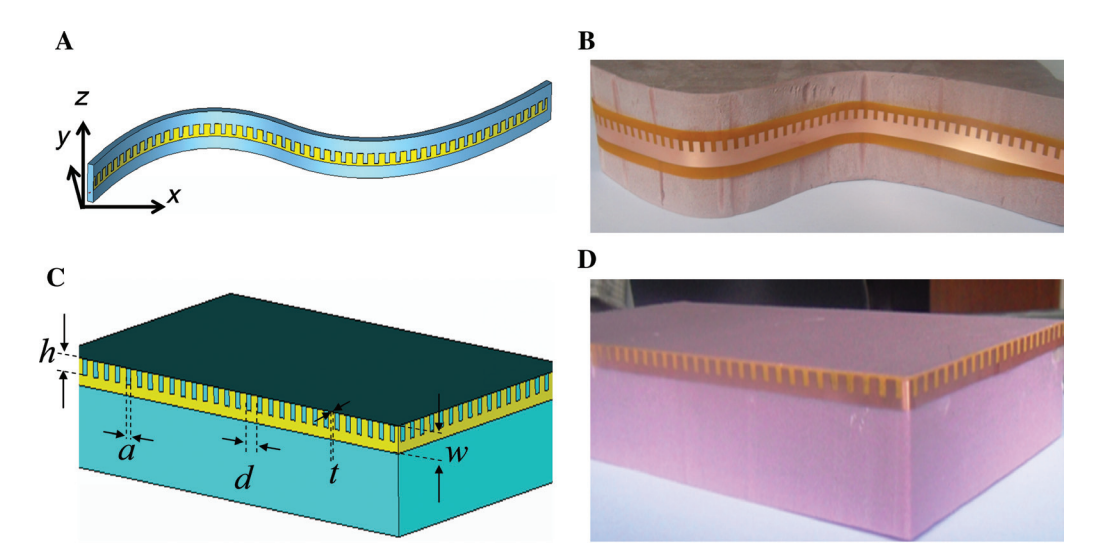


Figure 11: (A) and (B) Designed model and fabricated sample of smooth (S-bending) curved surface. (C, D) Designed model and fabricated sample of non-smooth (cubical) surface. Here, a=2 mm, d=5 mm, h=4 mm, w=5 mm, and t=0.018 mm.

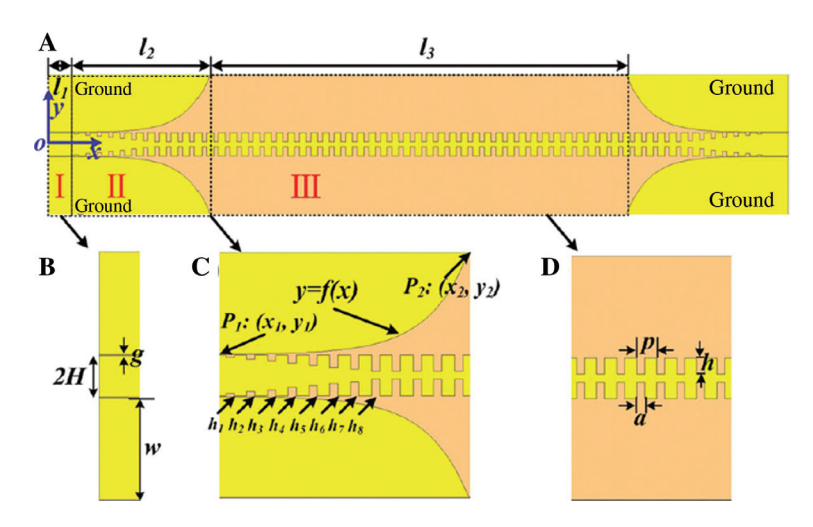


Figure 13: The configuration to bridge CPWs and plasmonic waveguide. (A) The hybrid CPW-plasmonic waveguide, in which $l_{i}=10$ mm, l_{\perp} =60 mm, and l_{\perp} =180 mm. (B) The CPW section, in which H=10 mm, w=25 mm, and q=0.4 mm. (C) The matching transition consisting of gradient grooves and flaring ground, in which $h_1=0.5$ mm, $h_2=1$ mm, $h_3=1.5$ mm, $h_4=2$ mm, $h_5=2.5$ mm, $h_6=3$ mm, $h_7=3.5$ mm, and $h_8=4$ mm. (D) The ultrathin corrugated metallic strip (the plasmonic waveguide) with p=5 mm, a=2 mm, and b=4 mm. Reproduced from [43] with permission.

However, as previously discussed, the k and k_0 have serious mismatch, especially when the frequency is close to the asymptotic frequency. In order to realize the wave vector matching between the plasmonic waveguide and the CPW, we have designed a transition to produce a gradient momentum. As shown in Figure 13C, the transition consists of a flaring ground and gradient grooves, in which the groove depth varies from $h_1 = 0.5$ mm to $h_2 = 4$ mm with a step of 0.5 mm, and the curve of flaring ground is described as $y = C_1 e^{\alpha x} + C_2 (x_1 < x_2)$, where $C_1 = \frac{y_2 - y_1}{e^{\alpha x_2} - e^{\alpha x_1}}$, $\alpha = 0.1$, and (x_1, y_1) , (x_2, y_2) are the start

and end points of the curve. In Figure 14, we give the

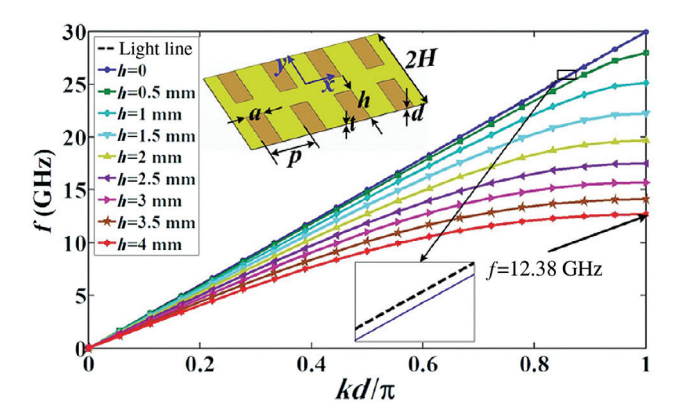


Figure 14: The dispersion curves of two-side metallic grooves with ultrathin thickness printed on a flexible dielectric film. The inset displays the corrugated metal plate with p=5 mm, a=2 mm, H=5 mm, t=0.018 mm, and d=0.05 mm. Reproduced from [43] with permission.

dispersion curves of the corrugated metal plate with a different groove depth, in which we clearly observe the wave vectors of SPPs at the same frequency, is gradually close to the wave vector in vacuum when groove depth decreases from 4 mm to 0 mm, realizing the matching of momentum from CPW (k_0) to the corrugated metallic strip (k).

For CPW parts, the signal transmission line is a bare single metallic line with zero groove depth, which makes very loose confinement of SPPs. The guided waves are completely confined by the ground of CPW. For the transition part, the mixed guided and SPP modes are supported. When the groove depth (h) is small, the confinement of SPPs is still loose, and the main modes are guided waves. Hence, the ground is still needed to confine the waves with high transmission efficiency. When the groove depth (h) becomes larger and larger, however, the guided waves are gradually transformed to SPPs, and the main modes are SPPs. In this case, the effect of the ground becomes very small, and hence, the ground can be flared out and terminated, and all waves are transformed to SPPs smoothly. On the other hand, in the flaring ground, the matching transition makes the impedance of CPW match gradually to the plasmonic waveguide.

We implement a microwave experiment to test the performance of the spoof SPP transducer. The sample is fabricated on an FCCL film with a thickness of 0.05 mm, as shown in Figure 15A. For such a plasmonic waveguide, the simulated and measured electric fields E_z at the frequency of 8 GHz are demonstrated in Figure 15B and C, which have excellent agreements. From these simulation and measured results, we observe that the smooth conversion

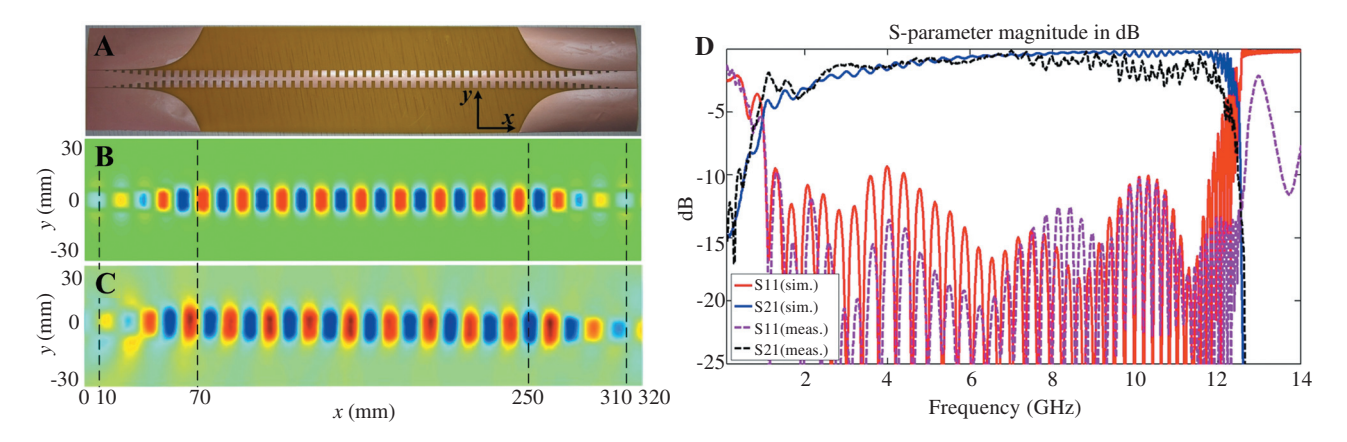


Figure 15: (A) Photo of the fabricated hybrid waveguide using FCCL. (B, C) Simulation and measured surface electric field of the hybrid waveguide, respectively. (D) The simulation and measurement S parameters of the hybrid waveguide with matching transition. Reproduced from [43] with permission.

between guided waves and spoof SPP wave appears. The conventional guided waves supported by the CPW have the main electric field along the *y*-axis direction, and therefore, the near fields of E_z are very small, as observed in the two ends of the plasmonic waveguide. Along the matching transition sections, the near fields of E_z increase gradually, and finally, the near E_z fields remain nearly constant. Undoubtedly, the guided waves in CPW have completely converted to spoof SPPs. In Figure 15D, we give the simulation and measurement S parameters of the plasmonic waveguide, from which we observe that S_{11} is lower than -10 dB, and S_{21} is higher than -0.6 dB from 6 GHz to 12 GHz. Moreover, we also observe that the cut-off frequency is 12.3 GHz in both simulation and measurement results, which is close to the asymptotic frequency (12.38 GHz) shown

in Figure 14. These results further demonstrate the highefficiency conversion from guided wave to SPP wave and propagation along the plasmonic waveguide with low loss.

Based on the high-efficiency conversion from guided waves to spoof SPPs, we can design a filter with specific function, as depicted in Figure 16 [44], which includes a straight plasmonic waveguide and electric field-coupled LC (ELC) resonator. Here, the grooves in the plasmonic waveguide is set to be protruded out of the inner conductor of CPW, and the ceiling of each groove is defined to be beveled, which makes the plasmonic waveguide have better SPP propagation characteristics than that shown in Figure 15A. The plasmonic waveguide is etched on a 0.5-mm-thick substrate with a dielectric constant of 2.65 and loss tangent of 0.003. The ELC particles are set with

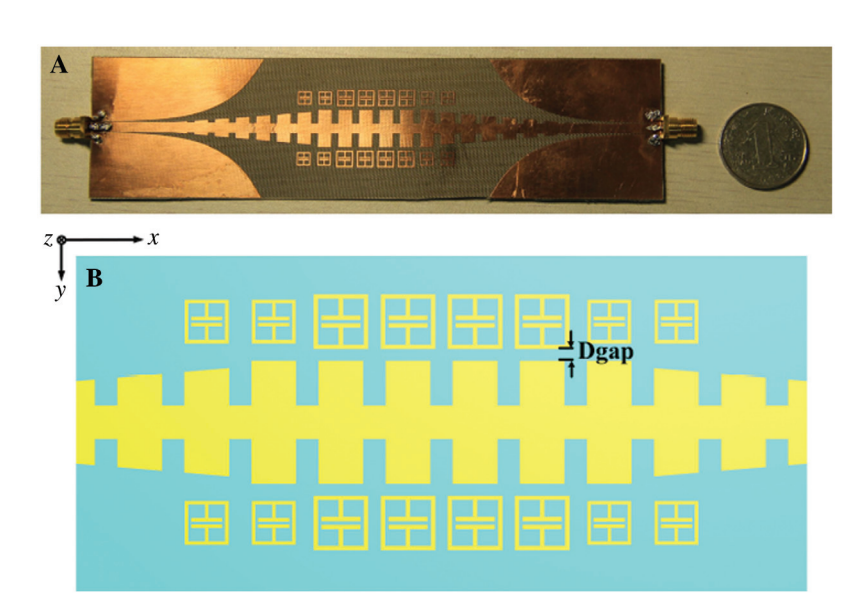


Figure 16: (A) The photograph of a fabricated sample for double-frequency rejections. (B) The schematic configuration of ELC array in the DFR SPP waveguide. Reproduced from [44] with permission.

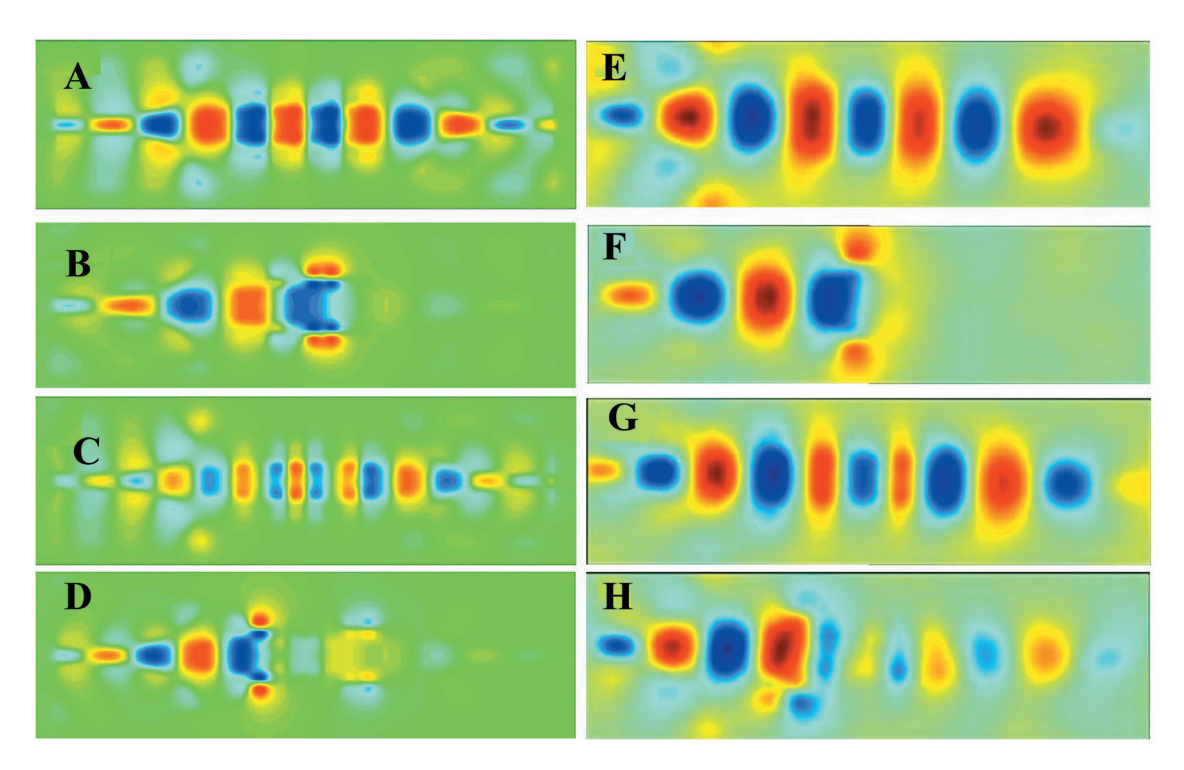


Figure 17: The near electric field distributions of the double-frequency rejection SPP waveguide at different frequencies. (A–D) The simulated results at 7.9 GHz, 7.65 GHz, 9.1 GHz, and 9.47 GHz. (E-H) The measured results at 7.9 GHz, 7.65 GHz, 9.1 GHz, and 9.47 GHz. Reproduced from [44] with permission.

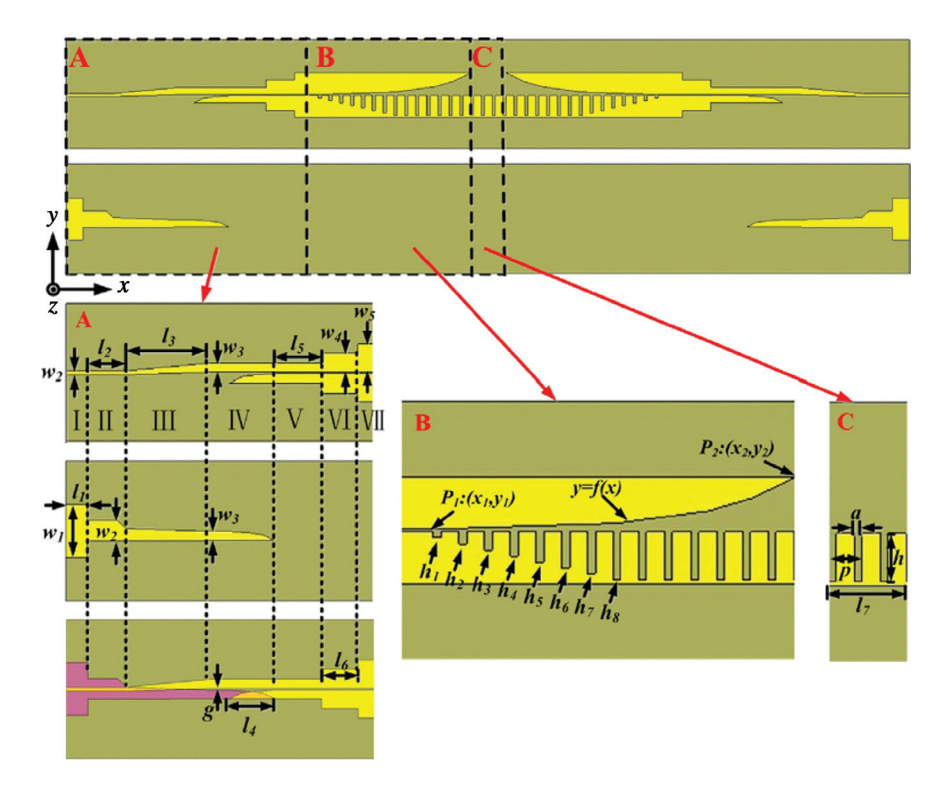


Figure 18: The sketch of back-to-back transition from microstrip to CSP waveguide. The transition divided into three regions (A, B, and C). The insets illustrate the detailed configurations of the three regions A, B, and C. Reproduced from [45] with permission.

their equivalent capacitors of two parallel metal lines along the x direction to achieve the strong resonances due to the existence of the y component of the SPP field. Such features provide a perfect absorption at the resonance frequency, which forms a rejection of SPP wave within a wide propagating band. Multifrequency and broadband frequency rejections can be realized by changing the size, number, and arrangement of ELC [44]. As shown in Figure 16, two dimensions of ELCs with scaling parameters k=0.7 and 0.8 are symmetrically located on both sides of the corrugated metal strip, in which a double-frequency rejection at 7.65 and 9.47 GHz appears. Simulation and measurement of near-electric field distributions are demonstrated in Figure 17. It is clearly seen that the SPP fields at rejection frequencies 7.65 and 9.47 GHz are cut-off at the places where the corresponding ELCs are resonant. For the non-resonant frequencies (7.9 and 9.1 GHz), the SPP fields are propagating through the ELC particles to the other end with almost no loss.

As mentioned above, for the corrugated metal plate with two-sided grooves (see Figures 13 and 16), the spoof SPP wave can be efficiently converted from the guided wave in CPW waveguide due to the symmetry of both CPW and plasmonic waveguide. For one-sided grooves, the symmetry is broken, and hence, the above transducer is hard to excite the spoof SPPs. To solve the problem, we also have designed a converter from microstrip to planar plasmonic waveguide [45], as shown in Figure 18. The first region including seven parts is a converter between the microstrip and plasmonic waveguide. The structure starts with a finite-ground-plane microstrip line typically with 50 Ω impedance, in which l_1 =7.7 mm, w_1 =19 mm, and w_2 =1.4 mm. In part two, the ground is designed as

 $l_2=14$ mm and $w_2=7.4$ mm to guide edge currents to the middle region. The part three is a transition section with length l_3 =3 mm, which is used to rotate the electric field by about 90°. The terminal widths in part three are both tuned to w_a =3.2 mm with a gap g=0.6 mm. The part four is an open circuit microstrip line and an open circuit CPS, whose terminals are overlapped on two sides of the substrate with length l_{\star} =16 mm. In part five, there is a 137- Ω coplanar strip (CPS) with strip width, gap, and length as 3.2 mm, 0.6 mm, and 17 mm, respectively. Part six with $l_c=13.2$ mm and $w_c=6.8$ mm is a quarter wave impedance transformer to provide good impedance matching between region A and the second region (region B). Part seven is a 120 Ω CPS with strip with w_c =10 mm and a gap of 0.6 mm. At last, the energy in the microstrip has been fed to the CPS, where the electric field direction is uniplanar. The CPS supports the quasi-TEM mode of guide waves with a wave number k_0 .

Region C is the plasmonic waveguide with length l_{γ} =355 mm, in which the period, width, and depth of grooves are designed as p=5 mm, a=1.5 mm, and h=9 mm, respectively. Figure 19A illustrates the dispersion curve of the spoof SPPs supported by the plasmonic waveguide. Attributing to the same cause as earlier, there is a big mismatch of wave number between the CPS and plasmonic waveguide. Therefore, a matching transition (region B) consisting of gradient groove depths and flaring metal line is used to match both the momentum and impedance between CPS and plasmonic waveguide. The groove depth increases from h_1 =1.1 mm to h_8 =8.8 mm with a 1.1-mm incremental step. The taper curve of the flaring metal line is determined by the same equation as Figure 13A, but different parameter α (here, α =0.06).

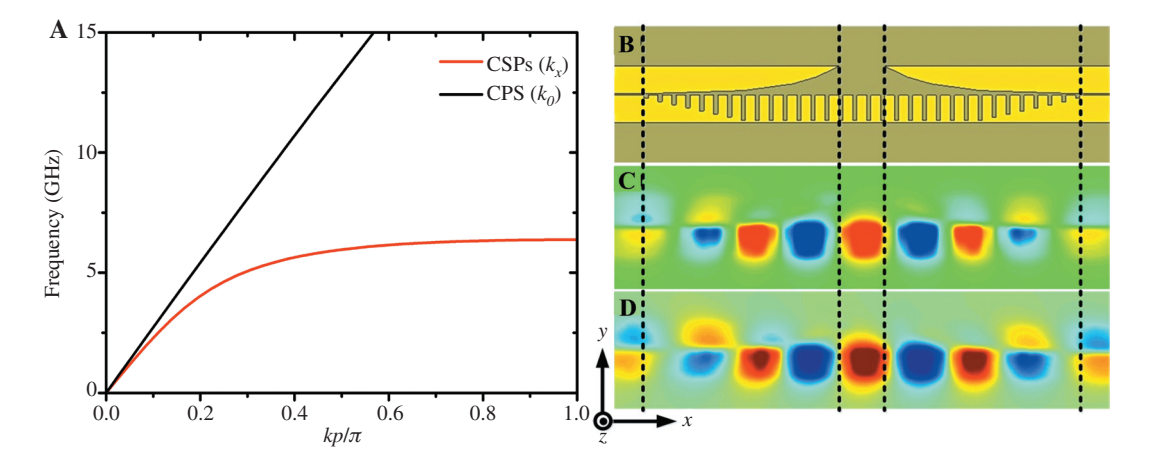


Figure 19: (A) Dispersion curves for the CPS and plasmonic waveguide, in which the red and black solid lines correspond to the CPS and plasmonic waveguide, respectively. (B) The matching transition between the CPS and plasmonic waveguide. (C-D) The simulated and measured *E*₂ field distributions at 4 GHz, respectively. Reproduced from [45] with permission.

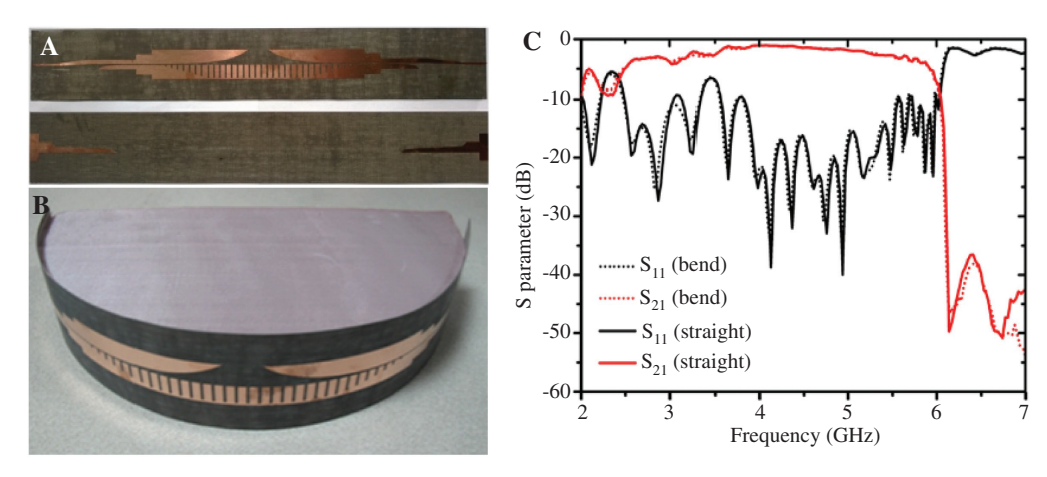


Figure 20: The photos of fabricated sample and measured S parameters. (A, B) The photos of the fabricated samples for the straight and bending SPP waveguides. (C) The measured S parameters for both the SPP waveguides. Reproduced from [45] with permission.

The full-wave simulation and measurement results of near-field E_z component are demonstrated in Figure 19C, D, which has excellent agreements. From these figures, we again observe that the small E_z components in the CPS section gradually increase along the matching transition sections, and then, constant amplitude is kept. The change process of the E_{\perp} fields again demonstrates that the guided waves in CPS are smoothly converted to the spoof SPP mode in the plasmonic waveguide.

Based on the above transducer, we have designed a straight and bending plasmonic waveguides. Figure 20A and B displays the fabricated sample, in which the bending plasmonic waveguide is pasted on a semicircle foam. The S parameters are simulated and measured to quantitatively evaluate their performance, as shown in Figure 20C. Obviously, the S parameters of a bending waveguide are completely coincidental with that of a straight waveguide, which demonstrate the very low bent loss. On the other hand, we observe that the -1-dB insertion bandwidth is from 3.8 GHz to 4.5 GHz, and the -3-dB insertion loss is from 3.2 GHz to 5.8 GHz, implying the high-efficiency transition of SPP and good transmission performance of the CSP waveguide.

5 Spoof localized surface plasmons

Besides the excellent SPP propagation characteristics of planar corrugated metal plate along arbitrarily curved surfaces, the spoof LSP field is very valuable to realize plasmonic sensors in the microwave or terahertz frequencies. For spoof LSP, the surface EM field is confined and strongly enhanced in the near vicinity of the plasmonic

particle interface, resulting in the LSP resonances being highly sensitive to the particle geometry and local dielectric environments. Here, we have designed a textured metallic disk to support spoof LSPs, as shown in Figure 21A, in which N periodically radical grooves are etched on a metal cylinder [46]. The outer and inner radii and the thickness of the textured disk are R, r, and t, respectively. The number of groove is defined as N=60, the inner radius is fixed as r=0.25R, and R=10 mm. When the thickness is very small (t=0.018 mm), the three dimension (3D) becomes a planar structure, as shown in Figure 20B.

The EM response of the planar structure has been verified by numerically simulating the extinction cross section (ECS), which includes absorption cross section (ACS) and scattering cross section (SCS). Figure 21D illustrates the simulation ECS spectrum, from which we see that there are multiple well-separated extinction peaks, indicating multiorder resonance excited on the planar textured metallic disk. The marked M₁–M₂ peaks in Figure 21D correspond to the excited LSP resonances, in which they correspond to the dipole (M₂), quadrupole (M₂), hexapole (M₂), octopole (M₂), decapole (M_c) , dodecapole (M_c) , and quattuordecapole (M_{π}) , respectively. To demonstrate it, the corresponding experiment and full-wave simulation of near-electric field distributions were conducted, in which a monopole is acted as the excitation of LSP. The fabricated sample of the planar plasmonic particle is illustrated in Figure 21C. The measured and simulated results are demonstrated in Figures 22 and 23, respectively, whose consistency of electric fields is very good except for the little deviations at resonant frequencies. The little deviations between the simulation results and experimental ones may be caused by two main reasons: one is the tolerance of fabrication; the other is the influence of the

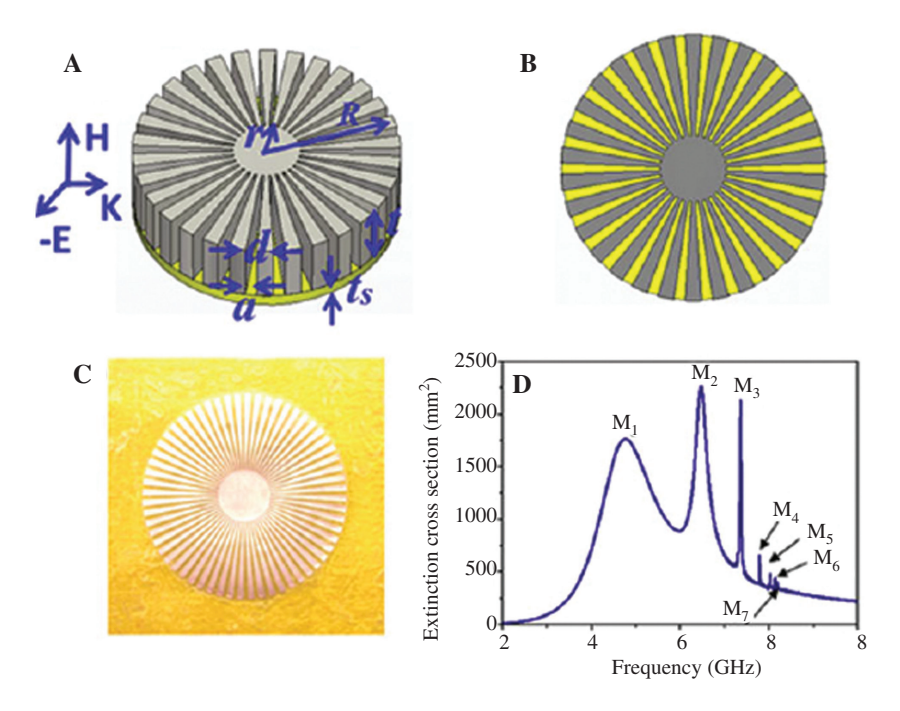


Figure 21: The textured metallic disk and the resonance properties. (A) A 3D structure with the inner and outer radii r and R, which is based on a thin dielectric substrate (yellow part) with thickness t_s . The thickness of the metallic disk (t) can be varied from infinity to nearly zero. (B) A planar textured structure. (C) The photograph of a fabricated planar textured metallic disk (t=0.018 mm) on a flexible dielectric substrate with thickness t_s =0.4 mm, in which t=10.0 mm, t=0.25t, t=0.4t, and t=60. (D) The simulated ECS spectra of the thin planar structure that has the same parameters as the fabricated sample. The marked t=0.4t=1 marked t=1 marked

excitation probe on the detector in the experiment because they do not have enough distance

An interesting physical phenomenon is that the spoof LSP modes on the planar textured disk are sensitive to the structural parameters and surrounding materials. All of the disk thickness, size, substrate, and number of grooves have significant impacts on LSP behaviors. As an example,

we have analyzed the influence of thickness (*t*) to the LSP resonances by full-wave simulation. Figure 24 represents the ECS spectra at different thickness: 0.018 to 1, 5, 10, 20, 30, and 40 mm. From this figure, we observe the following changes of LSP resonances: (1) the quality factor decreases, and all the resonant frequencies blue shift as the thickness increases; (2) the higher the resonance

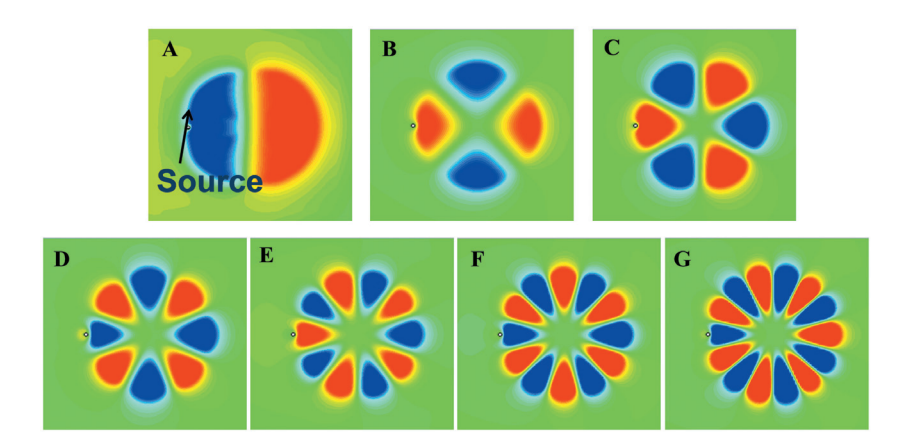


Figure 22: The simulated near-field patterns of vertical electric fields on a plane 0.5 mm above the textured metallic disk. (A) The dipole mode (M_1) at 4.75 GHz; (B) quadrupole mode (M_2) at 6.47 GHz; (C) hexapole mode (M_3) at 7.35 GHz; (D) octopole mode (M_4) at 7.77 GHz; (E) decapole mode (M_5) at 8.01 GHz; (F) dodecapole mode (M_6) at 8.11 GHz; (G) quattuordecapole mode (M_7) at 8.20 GHz. Reproduced from [46] with permission.

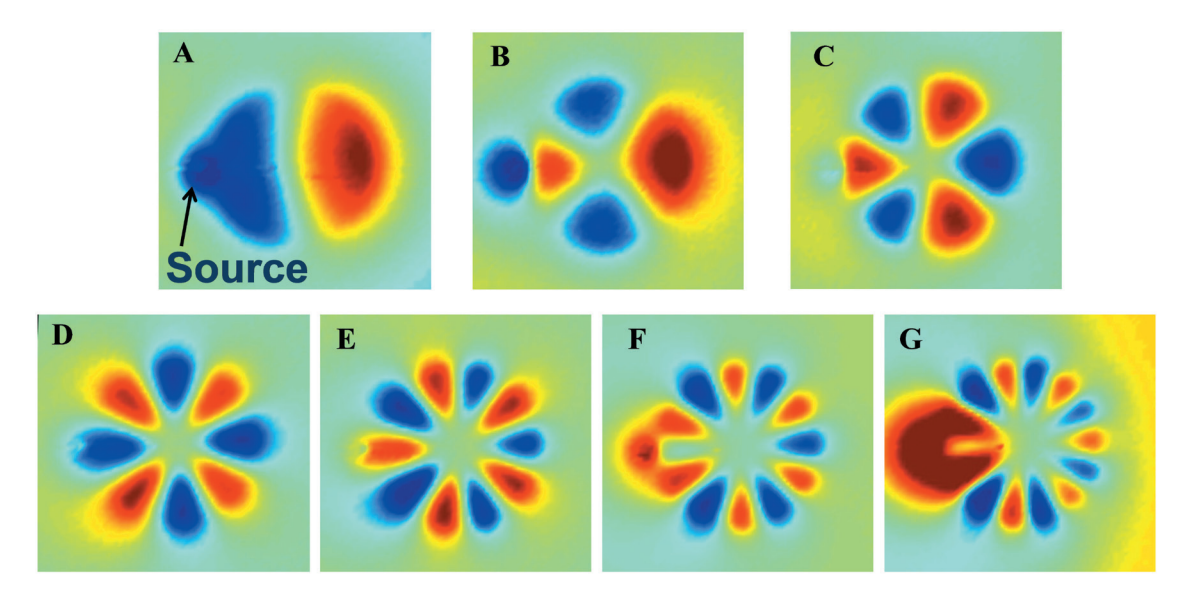


Figure 23: The measured near-field patterns of vertical electric fields on a plane 0.5 mm above the textured metallic disk, (A) Dipole mode (M.) at 4.52 GHz; (B) quadrupole mode (M.) at 6.24 GHz; (C) hexapole mode (M.) at 7.28 GHz; (D) octopole mode (M.) at 7.84 GHz; (E) decapole mode (M,) at 8.08 GHz; (F) dodecapole mode (M,) at 8.2 GHz; (G) quattuordecapole mode (M,) at 8.28 GHz. Reproduced from [46] with permission.

mode, the bigger the blue shift; (3) the width of the half maximum at each resonant peak becomes smaller as the thickness decreases; (4) the dipole resonance is weak at a disk thickness of 20 mm and nearly disappear when thickness increases to 40 mm; (5) as the thickness is even larger, the textured metal disk changes to a textured cylinder, which makes both dipole and quadrupole resonances disappear. It can be demonstrated in Figure 2 in Ref. [47]. These changes of LSP resonance for geometric parameters are many potential applications in microwave frequency. Especially for the change of surrounding materials, when

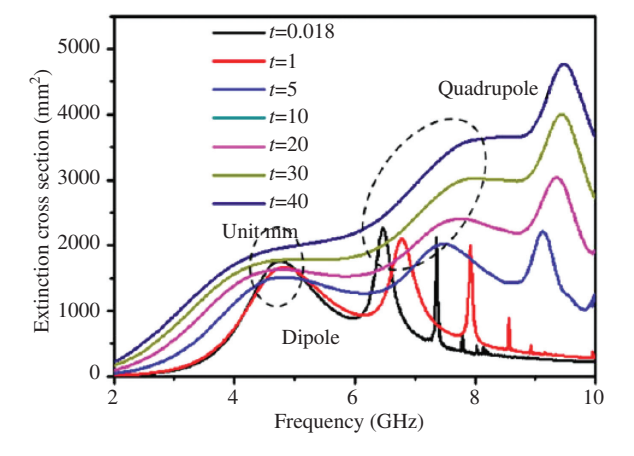


Figure 24: The impacts of disk thickness t on the LSP behaviors of the planar textured metallic disk, in which the thickness is defined as 0.018 to 1, 5, 10, 20, 30, and 40 mm, respectively. Reproduced from [46] with permission.

the refractive index of the detected material changes from 1 to 1.87, the resonant frequencies at quadrupole (M₃) and hexapole (M₂) modes shifts 0.5 GHz and 0.8 GHz, respectively, which makes it a good candidate for a microwave sensor to detect the surrounding materials [46].

We developed an analytical model, which is based on the modal expansion, to help obtain the physical insight [48]. The inset in Figure 25A gives the textured metal disk, in which the thickness is defined as infinite, and the other parameters such as R, r are coincident to that shown in Figure 21. The grooves are filled with a dielectric material of refractive index n_g . In this way, the resonant wavelengths λ_{res} can be made much larger than the object and create a deep subwavelength regime $R << \lambda_{roc}$. The EM fields in the outer region can be expanded in terms of the Hankel function of the first kind $H_n^{(1)}$, and considering that, for subwavelength particles, the field within the groove is given only by the fundamental waveguide mode. According to the matching of the EM modes outside the cylinder $(\rho > R)$ and inside the grooves $(r < \rho < R)$ by means of the appropriate boundary conditions at $\rho = R$, we obtain the following transcendental equation for the complex resonance frequency of the EM mode with azimuthal number *n*:

$$S_n^2 \frac{H_n^{(1)}(k_0 R)}{H_n^{(1)'}(k_0 R)} \tan(k_0 n_g h) = -n_g$$
 (1)

where $S_n = \sqrt{a/d} \operatorname{sinc}[n\pi a/(Nd)], H_n^{(1)'}(x) = dH_n^{(1)}(x)/dx$, and n_g is the refractive index filled in grooves. When an

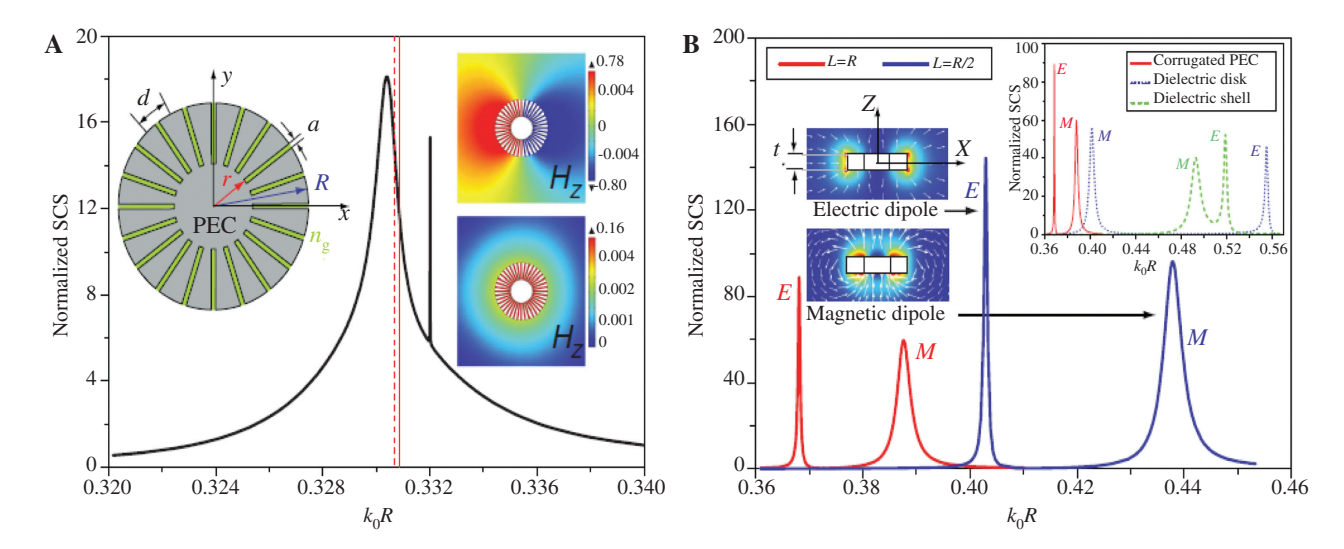


Figure 25: Magnetic LSPs in subwavelength metallic disk corrugated with dielectric grooves. (A) SCS for a 2D disk with r=0.4R, N=40, a/d=0.3, and $n_{\rm g}$ =8. The low-energy peak ($k_{\rm o}$ R=0.33) denotes two resonances: the electrical and magnetic dipoles, whose magnetic field amplitudes ($H_{\rm o}$) are shown in the upper and lower insets, respectively. The solid (dashed) vertical lines represent the position of the electric (magnetic) resonance obtained from the analytical model. (B) Textured metallic disk with finite thickness. The red and blue lines correspond to SCS for corrugated disks with thickness t=R and t=R/2, respectively. Top (and bottom) left insets: Near-field distribution of the electric field (and magnetic) dipole resonances for a disk of thickness t=R/2. The arrows show the electric (magnetic) field lines, and the color map shows the norm of electric (magnetic) field. Reproduced from [48] with permission.

integer number (n) of modal wavelengths fits into the perimeter, the resonance of the surface EM mode running around the cylinder surface appears. In the subwavelength limit, Eq. (1) predicts that the mode for n=0 (i.e., azimuthally independent) is very close in frequencies to the mode for n=1, as shown by the vertical lines in Figure 25A. On

the other hand, the analytical model can also be applied to estimate the LSP resonant type at resonance frequencies, for example, magnetic dipole LSP for the n=0 mode and electrical dipole LSP for the n=1 mode.

For the corrugated cylinder, when its length is reduced into a 3D corrugated disk (*t* is a finite value) or even planar

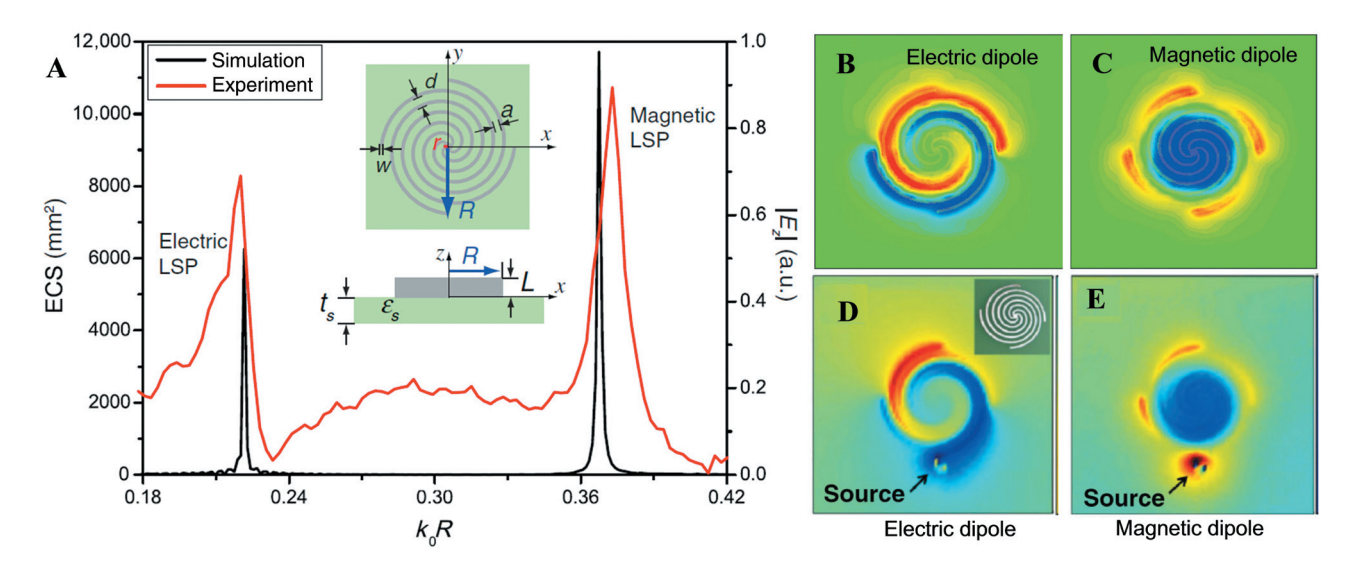


Figure 26: Resonance spectrum for subwavelength ultrathin metallic spiral structure. (A) Experimental near-field spectrum ($|E_z|$ is measured) and calculated ECS spectrum. The insets show a sketch of the structure, which is placed on top of a dielectric plate with thickness of 0.8 mm and dielectric constant of 3.5. The parameters are designed as r=9.5 mm, r=0.6 mm, d=1.508 mm, a=1.008 mm, and L=0.035 mm, respectively. (B, C) The simulated near-field distributions at the electric and magnetic LSPs, respectively, in an x-y plane 1.5 mm above the ultrathin disk. (D, E) The measured near-field patterns at the electric and magnetic LSPs, respectively. Reproduced from [48] with permission.

structure (t is very small, for example, 0.018 mm), we can observe an interesting phenomena, namely, resonances shift and splitting into magnetic and electric LSPs. Furthermore, the magnetic LSPs shift to higher frequencies than the electric LSPs. As an example, we have compared the SCS for two disks of different t (t=R and t=R/2) with grooves filled with a dielectric material (n_a =8). As shown in Figure 25B, two distinct peaks can be seen in the SCS plot for t=R (red line) and t=R/2 (blue line), in which the peak at a low frequency corresponds to the electric LSPs, while the one at a higher frequency is the magnetic LSPs (see the field distributions in inset in Figure 25B). It is worth noting that the magnetic LSPs are not observed in a corrugated disk with infinite length as the magnetic LSPs are very close in frequency to the electric LSPs.

The magnetic LSP modes appearing in the ultrathin textured disk are very promising to create dipolar magnetic resonance. These magnetic LSP modes rely on the dielectric material with very high n_{σ} in grooves, which could limit their feasible implementation. Hence, building up magnetic LSP modes supported by purely metallic structures would be much more convenient. From Eq. (1), we obtain the following conclusion: the complex resonance frequencies are mainly decided by the product $n_a h$. It implies that we can obtain magnetic LSP modes by replacing the groove filled with a dielectric material by a very long empty groove. Based on this idea, a PEC disk corrugated with meander or with spiral grooves can be used. As an example, here, we have designed and fabricated a planar textured disk with four spiral-shaped grooves (see the geometry sketch in Figure 26A), in which the four metallic spiral arms wrapped 1.5 turns around a small metallic disk of radius r such that the particle has an outer radius R. Each strip has width w, and two neighboring arms are separated by a distance d. The thickness of the textured copper disks is defined as L=0.035 mm, which is much smaller than the radius and, hence, looked as a planar structure. The whole ultrathin structure is fabricated on top of a FR4 substrate with thickness $t_{\rm s}$ =0.8 mm and dielectric permittivity 3.5. Full-wave simulation experiment for the extinction cross section (ECS) and near-field distributions have been conducted to demonstrate the existence of magnetic LSP mode. Figure 26B-E illustrates the simulation and experimental near fields of electric and magnetic dipoles.

The proposed planar LSPs can also be used to form Fano resonance, which is mainly based on the interference between the spectrally overlapping broad resonance and narrow discrete resonance [49]. As shown in Figure 27A, the multiple LSP resonances can be obtained in the ultrathin corrugated metallic disk when a horizontal polarized plane wave grazes its surface, while for a normally impinging plane wave, only broad electric dipole resonance is observed. Figure 27B illustrates the simulated ESC spectrum obtained from the plane wave illuminating the corrugated disk at the normal incidence and grazing incidence, which indicates the different LSP resonances. If the broad dipole resonance is looked as a bright mode, and these narrow discrete resonances are defined as dark modes, the Fano resonance will be observed when the dark modes couple EM energies from the bright mode.

To demonstrate it, we have designed a LSP dimmer, as shown in Figure 28A, in which two asymmetrically metallic disks with R_1 =10.5 mm, R_2 =8.5 mm, r_1 = r_2 =2 mm (for the other parameters, see Figure 27A) are placed in close proximity. The Fano resonance has been verified by simulating the ECS spectrum. Figure 28B represents the ECS spectra for the dimer (black solid line), the small disk (blue dashed line), and the big disk (red dotted line), respectively. From these

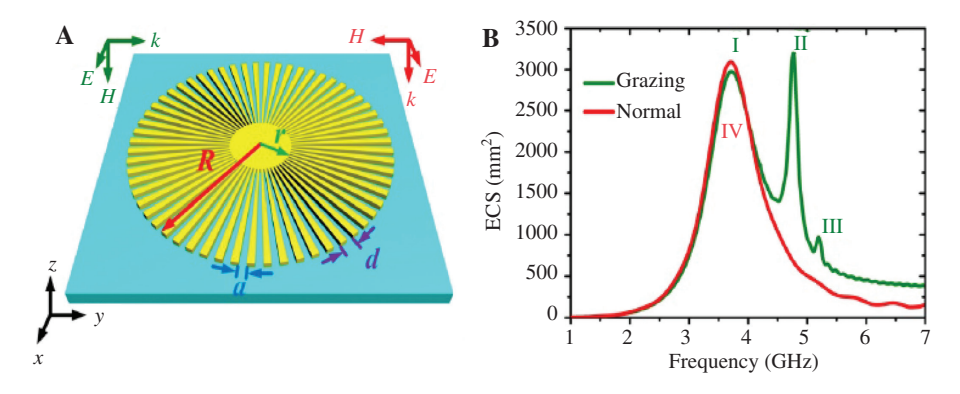


Figure 27: Textured metallic disk and the resonance properties. (A) Ultrathin spoof LSP structure based on a thin dielectric substrate, in which R=10.5 mm, r=2 mm, d=1.1 mm, a=0.55 mm, and the number of grooves N=60. (B) The simulation ECS spectra for grazing and normal incidences. The green and red lines correspond to the grazing and normal incidence, respectively. Reproduced from [49] with permission.

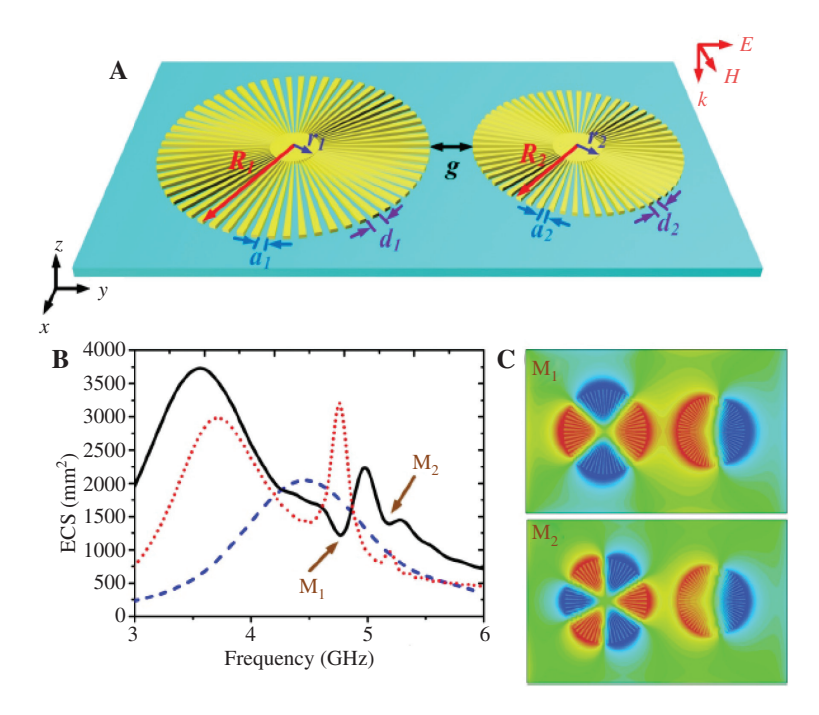


Figure 28: The schematic picture of the ultrathin LSP dimer and the multiple Fano resonance. (A) The configuration of the LSP dimer. (B) The simulated ECS spectra for the LSP dimer and individual LSP disks. The black solid line corresponds to the LSP dimer, where the dips are marked as M_1 and M_2 . The red dotted line denotes the big disk, which is illuminated by gazing incidence. The blue dashed line corresponds to the small disk, which is illuminated by normal incidence. (C) Simulation results of the near-field (E_2) distributions at the resonance frequencies M_1 and M_2 . Reproduced from [49] with permission.

spectra, we observe the multiple Fano line shape from 4 GHz to 6 GHz (see black solid line), which is the spectral overlap between the broad dipole mode (bright mode corresponds to blue dashed line) and the narrow multiple modes (dark modes correspond to the second and the third resonance in red dotted line). We remark that the spectral position of dips are in good agreements with the multipolar resonances (red dotted line), implying the multiple Fano resonance of the dimer originating from the destructive interference between the bright dipole mode of the smaller particle and the dark multipole modes of the larger particle. The simulated nearfield (E_{z}) distributions at the dips M₁ and M₂, as illustrated in Figure 28C, demonstrate the coupling between the dipole mode of the small disk and the quadrupole and hexapole modes of the big disk, showing the dark modes (big disk) excited by the bright mode (small disk).

6 Conclusions

In this review, we briefly introduce the characteristics of surface wave in ultrathin plasmonic metamaterial under three scenarios: the spoof SPP propagation, the spoof SPP excitation, and the spoof LSP. Their advantages are given in the context of practical implementation. Using these techniques, several applications including plasmonic waveguides (planar and conformal structures), plasmonic filters (planar and bending structures), electric LSPs and magnetic LSPs, and Fano resonance are given to demonstrate the powerfulness of the planar plasmonic metamaterial. We believe that the planar metamaterials are probable to be extended to optical frequency to produce the high-performance planar plasmonic devices, integrated circuits and systems.

Acknowledgments: This work was supported by the National Science Foundation of China (61461016, 61138001, 61171024, 61171026, 61201083, 61361005, and 61161002), National High Tech (863) Projects (2012AA030402 and 2011AA010202), 111 Project (111-2-05), Guangxi Experiment Center of Information Science (20130330 and 20130202), Postdoctoral Science Foundation of China (No.2013M531250), Natural Science Foundation of Guangxi (2014GXNSFAA118366 and 2012GXNSFAA053233).

References

[1] Maier SA. *Plasmonics: Fundamental and Applications*, Springer: New York, 2007.

- [2] Heinz R. Surface Plasmons on Smooth Surfaces, Springer: Berlin Heidelberg, 1988.
- [3] Bostwick A, Speck F, Seyller T, Horn K, Polini M, Asgari R, Mac-Donald AH, Rotenberg E. Observation of plasmarons in quasifreestanding doped graphene. Science 2010, 328, 999-1002.
- [4] Gramotnev DK, Bozhevolnyi SI. Plasmonic beyond the diffraction limit. Nat. Photonics 2010, 4, 83-91.
- [5] Ebbesen TW, Genet C, Bozhevolnyi SI. Surface-plasmon circuitry. Phys. Today 2008, 61, 44-50.
- [6] Nagpal P, Lindquist NC, Oh SH, Norris DJ. Ultrasmooth patterned metals for plasmonic and metamaterials. Science 2009, 325, 594-597.
- [7] Barnes WL, Dereux A, Ebbesen TW. Surface plasmon subwaveglength optics. Nature 2003, 424, 824-830.
- [8] Bozhevolnyi SI, Volkov VS, Devaux E, Laluet JY, Ebbesen TW. Channel plasmon subwavelength waveguide components including interferometers and ring resonators. Nature 2006, 440,508-511.
- [9] Volkov VS, Bozhevolnyi SI, Devaux E, Laluet JY, Ebbesen TW. Wavelength selective nanophotonic components utilizing channel plasmon polaritons. Nano Lett. 2007, 7, 880-884.
- [10] Zia R, Schuller JA, Chandran A, Brongersma ML. Plasmonics: the next chip-scale technology. Mater. Today 2006, 9, 20-27.
- [11] Fang N, Lee H, Sun C, Zhang X. Sub-diffraction-limited optical imaging with a sliver superlens. Science 2006, 308, 534-537.
- [12] Polman A, Atwater HA. Photonic design principles for ultrahigh-efficiency photovoltaics. Nat. Mater. 2012, 11, 174-177.
- [13] Ozbay E. Plasmonics: merging photonics and electronics at nanoscale dimensions. Science 2006, 311, 189-193.
- [14] Javier Garcia de Abajo F. Graphene nanophotonics. Science 2013, 339, 917-918.
- [15] Goubau G. Surface waves and their application to transmission lines. J. Appl. Phys. 1950, 21, 1119-1128.
- [16] Wait JR. The ancient and modern history of EM ground-wave propagation. IEEE Antennas. Propag. 1998, 40, 7-24.
- [17] Wachter M, Nagel M, Kurz H. Frequency-dependent characterization of THz Sommerfeld wave propagtion in single-wires. Opt. Express 2005, 13, 108815-10822.
- [18] Pendry JB, Martin-Moreno L, Garcia-Vidal FJ. Mimicking surface plasmons with structured surfaces. Science 2004, 305, 847–848.
- [19] Hibbins AP, Evans BR, Sambles JR. Experimental verification of designer suerface plasmons. Science 2005, 308, 670-672.
- [20] Garcica-Vidal FJ, Martin-Meoreno L, Pendery JB. Surfaces with holes in them: new plasmonic metamaterials. J. Opt. A-Pure Appl. Op. 2005, 7, S97-S101.
- [21] Gan Q, Gao Y, Wagner K, Vezenov D, Ding YJ, Bartoli FJ. Experimental verification of the rainbow trapping effect in adiabatic plasmonic gratings. Proc. Natl. Acad. Sci. 2011, 108, 5169-5173.
- [22] Gan Q, Fu Z, Ding YJ, Bartoli FJ. Ultrawide-bandwidth slow-light system based on THz plasmonic graded metallic grating structures. Phys. Rev. Lett. 2008, 100, 256803.
- [23] Jiang T, Shen LF, Wu JJ, Jin J; Yang T-J, Ruan Z, Ran L. Realization of tightly confined channel plasmon polaritons at low frequencies. Appl. Phys. Lett. 2011, 99, 261103.
- [24] Gao X, Shi JH, Ma HF, Jiang WX, Cui TJ. Dual-band spoof surface plasmon polaritons based on composite-periodic gratings. J. Phys. D: Appl. Phys. 2012, 45, 505104.
- [25] Yu N, Wang QJ, Kats MA, Fan JA, Khanna SP, Li L, Davies AG, Linfield EH, Capasso F. Designer spoof plasmon structures collimate Terahertz Laser Beams. Nat. Mater. 2010, 9, 730-735.

- [26] Brock EMG, Hendry E, Hibbins AP. Subwavelength lateral confinement of microwave surface waves. Appl. Phys. Lett. 2011, 99, 051108.
- [27] Martin-Can D, Nesterov ML, Fernandez-Dominguez Al, Garcia-Vidal FJ, Martin-Moreno L, Moreno E. Domina plasmons for subwavelength terahertz circuitry. Opt. Express 2010, 18, 754-764.
- [28] Maier SA, Andrews SR, Martin-Morene L, Garcia-Vidal FJ. Terahertz surface plasmon-polaritons propagation and focusing on periodically corrugated metal wires. Phys. Rev. Lett. 2006, 97, 176805.
- [29] Zhou YJ, Cui TJ. Multidirectional surface-wave splitters. Appl. Phys. Lett. 2011, 98, 221901.
- [30] Zhou YJ, Jiang Q, Cui TJ. Bidirectional bending splitter of designer surface plasmons, Appl. Phys. Lett. 2011, 99, 101904.
- [31] Tang YB, Wang ZC, Wosinski L, Westergren U, He S. Highly efficient non-uniform grating coupler for silicon-on-insulator nanophotonic circuits. Opt. Lett. 2010, 35, 1290-1292.
- [32] Sun S, He Q, Xiao S, Xu Q, Li X, Zhou L. Gradient-index metasurfaces as a bridge linking propagating waves and surface waves. Nature Mater. 2012, 11, 426-431.
- [33] Treizebre A, Aalin T, Bocquet B. Planar excitation of Goubau transmission lines for THz BioMEMS. IEEE Microw. Wire. Compon. Lett. 2005, 15, 886-888.
- [34] Akalin T, Treizebre A, Bocquet B. Single-wire transmission lines at terahertz frequencies. IEEE Trans. Microw. Theory Tech. 2006, 54, 2762-2767.
- [35] Chen WC, Mock JJ, Smith DR, Akalin T, Padilla WJ. Controlling gigahertz and terahertz surface electromagnetic waves with metamaterial resonators. Phys. Rev. X 2011, 1, 021016.
- [36] Zhou YJ, Jiang Q, Cui TJ. Bidirectional surface wave splitters excited by a cylindrical wire. Opt. Express 2011, 19, 5260-5267.
- [37] Zhou YJ, Cui TJ. Broadband slow-wave systems of subwavelength thickness excited by a metal wire. Appl. Phys. Lett. 2011, 99, 101906.
- [38] Zhou YJ, Jiang Q, Cui TJ. Three-dimensional subwavelength components utilizing THz surface plasmons. Sci. China Inform. Sci. 2012, 55, 79-89.
- [39] Shen X, Cui TJ. Planar plasmonic metamaterial on a thin film with nearly zero thickness. Appl. Phys. Lett. 2013, 102, 211909.
- [40] Shen XP, Cui TJ, Martin-Cano D, Garcia-Vidal FJ. Conformal surface propagation on ultrathin and flexible films. Proc. Natl. Acad. Sci. 2013, 110, 40-45.
- [41] Gao X, Zhou L, Liao Z, Ma HF, Cui TJ. An ultra-wideband surface plasmonic filter in microwave frequency. Appl. Phys. Lett. 2014, 104, 191603.
- [42] Gao X, Shi JH, Shen XP, Ma HF, Jiang WX, Li LM, Cui TJ. Ultrathin dual-band surface plasmonic polariton waveguide and frequency splitter in microwave frequencies. Appl. Phys. Lett. 2013, 102, 151912.
- [43] Ma HF, Shen XP, Cheng Q, Jiang WX, Cui TJ. Broadband and high-efficiency conversion from guided waves to spoof surface plasmon polaritons. Laser Photonics Rev. 2014, 8, 146-151.
- [44] Pan BC, Liao Z, Zhao J, Cui TJ. Controlling rejections of spoof surface plasmon polaritons using metamaterial particles. Opt. Express 2014, 22, 13940-13950.
- [45] Liao Z, Zhao J, Pan BC, Shen XP, Cui TJ. Broadband transition between microstrip line and conformal surface plasmon waveguide. J. Phys. D: Appl. Phys. 2014, 47, 315103.

- [46] Shen XP, Cui TJ. Ultrathin plasmonic metamaterial for spoof localized surface plasmons. Laser Photonics Rev. 2014, 8, 137-145.
- [47] Pors A, Moreno E, Moreno LM, Pendry JB, Garcia-Vidal FJ. Localized spoof plasmons arise while texturing closed surfaces. Phys. Rev. Lett. 2012, 108, 223905.
- [48] Huidobro PA, Shen XP, Cuerda J, Moreno E, Moreno M, Garcia-Vidal FJ, Cui TJ, Pendry JB. Magnetic localized surface plasmons. Phys. Rev. X 2014, 4, 021003.
- [49] Liao Z, Pan BC, Shen XP, Cui TJ. Multiple Fano resonances in spoof localized surface plasmons. Opt. Express 2014, 22, 15710-15717.

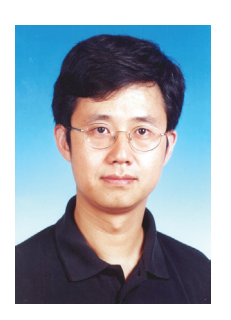
Bionotes



Xi Gao

State Key Laboratory of Millimeter Waves, Department of Radio Engineering, Southeast University, Nanjing 210096, People's Republic of China; and School of Information and Communication, Guilin University of Electronic Technology, Guilin 541004, People's Republic of China

Xi Gao received his PhD degree at University of Electronic Science and Technology of China (UESTC), Chengdu, China, in 2009. He was a Postdoctoral Researcher (2011-2014) in the Department of Radio Engineering, Southeast University, Nanjing, China. Since 2010, he has joined in the School of Information and Communication, Guilin University of Electronic Technology, Guilin, China. His research interests include metamaterials and antenna design.



Tie Jun Cui State Key Laboratory of Millimeter Waves, Department of Radio Engineering, Southeast University, Nanjing 210096, People's Republic of China tjcui@seu.edu.cn

Tie Jun Cui received his PhD degree at Xidian University, Xi'an, China, in 1993. He was an Alexander von Humboldt Foundation Research Fellow at the University of Karlsruhe, Germany (2005-2007), a Postdoctoral Research Associate (1997-2000) and Research Scientist (2001-2002) at the University of Illinois at Urbana-Champaign, USA. Since 2002, he has joined in the Department of Radio Engineering, Southeast University, Nanjing, China, as a Cheung-Kong Professor. Dr. Cui is a Co-Editor of the book Metamaterials – Theory, Design, and Applications (2009), and has published over 200 peer-review journal papers with more than 9500 citations. His research interests include metamaterials, computational electromagnetics, and millimeter wave technologies.